Controls on generation and accumulation of blended gases (CH4/H2/He) in the Neoproterozoic Amadeus Basin, Australia

Mahmoud Leila, Keanu Loiseau, Isabelle Moretti

Controls on generation and accumulation of blended gases (CH_4/H_2/He) in the Neoproterozoic Amadeus Basin, Australia.

Mahmoud Leila[a,b*], **Keanu Loiseau**[a], **Isabelle Moretti**[a]

[a]Laboratoire des Fluides Complexes et leurs Réservoirs, Université de Pau et des pays de l'Adour, France
[b]Geology Department, Faculty of Science, Mansoura University, Egypt
*Corresponding author: Mahmoud_lotfy@mans.edu.eg

Abstract

Various gases are generated in the subsurface, by diagenetic processes, fluid/rock interactions, maturation of petroleum source rocks and microbial activity. Often these gases just leak at the surface but sometimes they may accumulate in a subsurface trap. The present study investigates the case of the southern part of the Amadeus Basin, Australia, where exploration wells tested a blend of hydrocarbon (HC), helium (He) and hydrogen (H_2). In Mt Kitty-1 well, He- and H_2-rich gases were reported (He ~9%, H_2 ~11.4%) with traces of HC, whereas C_1 and C_{2+} HC gases associated with He were discovered in Magee-1 well. Seismic and well data elucidate accumulation of the gas blend within a classical subsurface system with a structural trap, a permeable reservoir and a thick salt layer as seal. This salt, the Proterozoic Upper Gillen, is overlying the Heavitree sandstones and fractured basement reservoirs. The former is dominated by intergranular porosity (~13%), whereas the latter is commonly associated with complex patterns of fractures associated with deep-seated faults. The sources of blended gases are different: thermal cracking of organic matter for hydrocarbons, radiolytic decay of radioelements for helium. Radiolysis, and water reduction as well as oxidation of hydrocarbons are open hypothesizes for H_2 generation in the study region. Neoproterozoic and Early Paleozoic tectonic episodes (e.g. Petermann; Alice Springs) allowed the formation of various structural traps where the gas blend was accumulated.

The large quantity of He, light gas slowly generated by the crustal radioactivity indicates that the seal is very efficient and that accumulations could have been in place for millions of years very likely with an evolving CH_4/H_2/He ratios through time. The presence of gas chimneys and surface depressions in the basin indicate that the generation, and/or migration of the gases are still active. All the data are consistent with

a long-term accumulation of this gas blend, different from the short term H_2 retention in the reservoir that was proposed in other contexts such as in Mali.

Keywords: Natural hydrogen; helium; hydrocarbon gases; Amadeus Basin; Australia.

1. Introduction

Generation of hydrocarbon and non-hydrocarbon gases is mostly dependent on the complex interactions between three main genetic processes (biogenesis, thermogenesis and abiogenesis) (Bernard, 1978; Schoell, 1983; Whiticar, 1999; Lin et al., 2005; Vacquand et al., 2018 and references therein). Deciphering the origin of these gases and various mechanisms of their generation is crucial for a proper exploitation of the geo-resources. Hydrocarbons (HC) are often expelled from thermally-mature organic-rich rocks after reaching the oil and gas window maturities, whereas biogenic processes commonly generate dry HC by consuming the light liquid HC phases at low temperature levels (Schoell, 1983; Peters and Casa, 1994; Whiticar, 1999; Leila and Moscariello, 2017). Radiolysis also generates helium (He) and hydrogen (H_2) gases via the radiolytic decay of radioelements coupled with a possible dissociation of water (Ballentine et al., 1991; Warr et al., 2019, Klein et al., 2019 and references therein). The abiogenic processes can produce light hydrocarbon (mainly C_1 and C_{2+}) and non-hydrocarbon (H_2, CO_2) gases at a wide range of temperatures in various geological environments (Coveney et al., 1987; Holloway and O'Day, 2000; Taran et al., 2010; Etiope, 2017; Prinzhofer et al., 2019; Moretti et al., 2021a, b; Leila et al., 2021; Radwan et al., 2022). These processes include redox reactions between water and Fe^{+2}-bearing rocks (mafic, ultramafic rocks and ironstones) (Charlou et al., 2002; McCollom and Bach, 2009; Vacquand et al., 2018), radiolytic dissociation of water by radioelements (uranium, thorium) in crustal rocks (Lin et al., 2005; Sherwood Lollar et al., 2014), volcanism and volcanic degassing (Stefánsson and Arnórsson, 2002) as well as thermal metamorphism (Orlando et al., 2010).

Natural H_2 generation via abiogenic processes was recently estimated at 2.8 M-tonnes/year (Truche et al., 2020), nonetheless, this estimation could be much more under-estimated (Zgonnik, 2020). Moreover, recent discovery of shallow H_2-rich (~98 mol%) gas in Bougou-1 well, Taoudeni Basin, in Mali (Prinzhofer et al., 2018), highlights the potentiality of subsurface natural H_2 exploitation. Just a few years ago, it was

63 claimed that H_2 does not exist as a free gas in the Earth's crust and the fact that a
64 natural seal did not exist for such a low molecular weight gas was often affirmed and
65 published (e.g. Zgonnik et al., 2015; Moretti et al., 2021a, b). The implications of the
66 subsurface H_2 storage and of the discovery in Mali was not really considered.
67 Additionally, some geoscientists believe that the subsurface H_2 will be mainly produced
68 within a dynamic system and a flow of H_2 may exists in a porous medium such as in
69 Mali (Prinzhofer et al., 2018) or within the steam of the geothermal plans (Stefánsson
70 and Arnórsson, 2002; Combaudon et al., 2022). Hydrogen currently presents a zero
71 carbon alternative for the traditional fossil fuels and the advances in H_2 exploration and
72 production may aid in the decarbonization of the global energy supply (e.g. Gielen et al.,
73 2019). Similarly, other non-HC gases such as helium is widely used in high-tech
74 industries such as cryogenics, and the global demand for this important gas is currently
75 increasing (Skirrow et al., 2013; Waltenberg, 2015; Haines and Allen, 2019).

76 Blended hydrocarbon and non-hydrocarbon gases were reported from several
77 places in Australia such as the Cobar copper mine, New South Wales (~75% H_2 and ~
78 25% CH_4; Stack and Rabone, 2018), Yorke Peninsula and Kangaroo Island
79 (Woolnough, 1934) as well as in some exploration wells offshore Victoria (Golden
80 Beach-1 ~38 mol.% H_2) and in Amadeus Basin (Mt. Kitty-1 ~11 mol.% H_2) (McInnes et
81 al., 2017). In addition, surficial evidence for subsurface gas emanations is recognized
82 by sub-circular depressions (SCD) that have been reported from all over the globe
83 (Russia, USA, Brazil, and Ukraine) (Larin et al., 2015; Zgonnik et al., 2015, Prinzhofer et
84 al., 2019; Zgonnik, 2020; Moretti et al., 2021a, b, Geymond et al., 2022). They are
85 visible on satellite images and have been observed in several places in Australia where
86 seeps of H_2-rich gases have been reported (Moretti et al., 2021b, Frery et al, 2021).

87 The present study focuses on the HC and non-HC gas blend discovered in the
88 Amadeus Basin, central Australia (Fig. 1). The Amadeus Basin is an extensive
89 intracratonic structure covering an area of approximately 170,000 km^2. It is one of the
90 Australia's most petroliferous provinces with hydrocarbon exploration history that has
91 been started since the early 1960s (Young and Ambrose, 2007). The basin contains
92 proven HC reserves estimated at approximately 37 million barrels of oil and more than
93 400 BCF (billion cubic feet) of gases (Jackson et al., 1984). It constitutes a thick (~ 17

km) sedimentary cover of Proterozoic to late Devonian rocks (Fig. 2). Five distinct petroleum systems have been identified in the Amadeus Basin; the first four are mainly hosted in the Neoproterozoic rocks with sub-economic gas discoveries (e.g. Magee-1, Mereenie, Orange-1, -2 and Dingo-1 to -5).

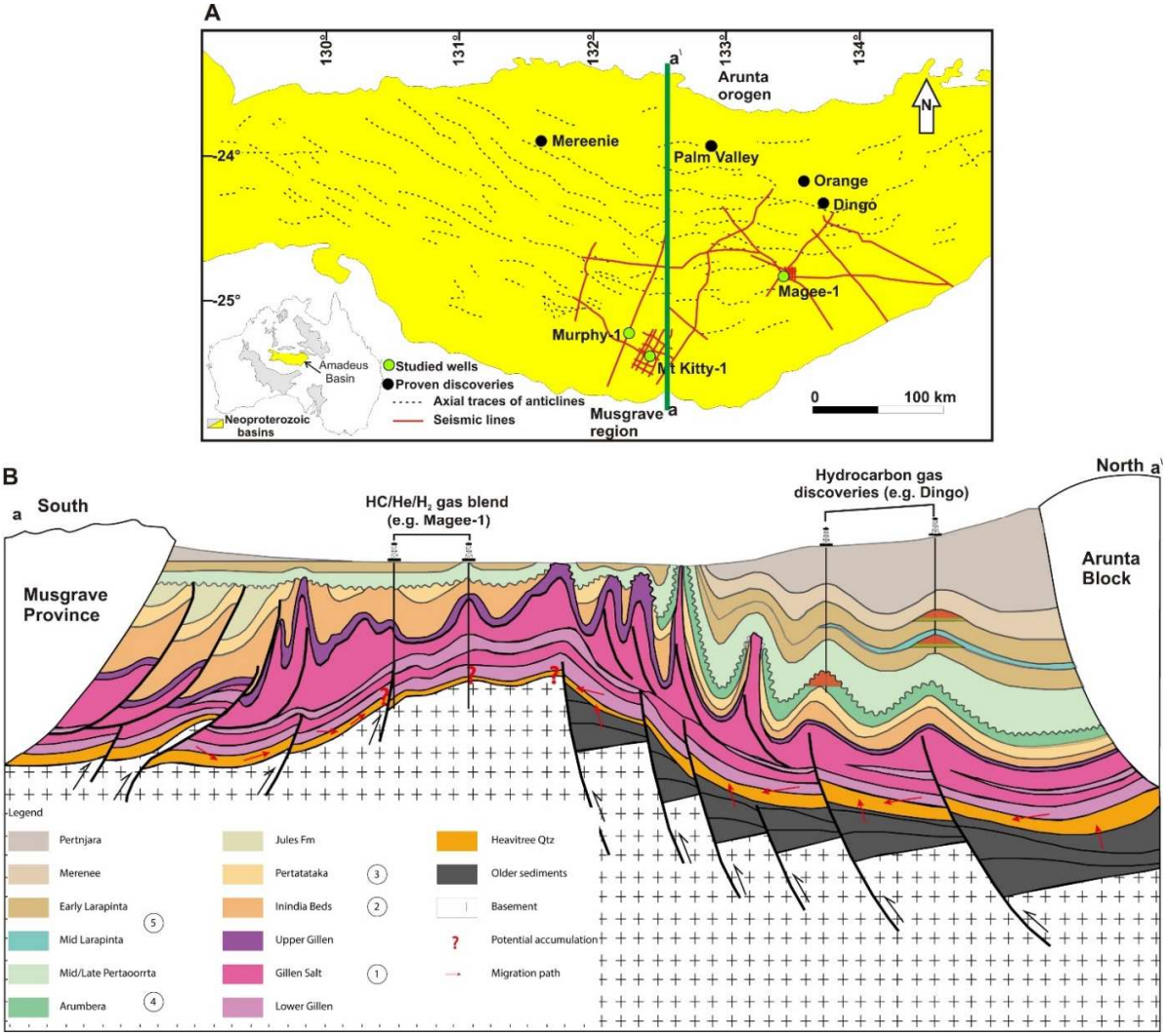

Fig. 1. A) Location map illustrating the location of the studied wells and proven gas discoveries in Amadeus Basin, central Australia, B) Illustrative N-S cross-section (not to scale) in central Amadeus Basin showing the main structural elements, the distribution of different stratigraphic units (modified from Johns et al., 2017) and the kind of plays that have been targeted.

The youngest petroleum system comprises the Ordovician sandstones hosting the economic accumulations of large oil and gas such as the Mereenie and Palm Valley

fields (Fig. 1; Marshall, 2003). The source rock potential of the Neoproterozoic systems was considered to be poor or rather negligible (Jackson et al., 1984; Summons and Powell, 1991). However, the recent organic-geochemical and geologic data have demonstrated several potential source rocks in the Neoproterozoic successions in some parts of the basin (Marshall, 2003; 2004). Today, the non-hydrocarbon gas plays (H_2, He) in the Neoproterozoic systems are actively explored (Hissey et al., 2016; Scrimgeour, 2019; Haines and Allen, 2019). The case of HC/He/H_2 gas blend in the Amadeus Basin is especially interesting since their kinetics are rather different and the gases have variable residence times in the reservoir (Lin et al., 2005). The factors controlling the generation, mixing and accumulation of this gas blend remain poorly constrained but in Australia the subsurface data are publicly available and we took this opportunity to investigate the surface and subsurface data, seismic and wells for potential geo-energy exploration plans. Additionally, with proven resources of both HC and non-HC gases, Amadeus Basin presents a natural laboratory where we can examine the controls on generation and accumulation of various gas plays.

2. Geologic setting

The Amadeus Basin presents an E-W trending belt of folded Neoproterozoic-Early Paleozoic (Cambrian-Devonian) sedimentary successions in central Australia overlying unconformably the Paleo- to Mesoproterozoic crystalline basement complex (Wells et al., 1970; Jackson et al., 1984; Marshall et al., 2007; Edgoose, 2013; Carr et al., 2016). The basement rocks are exposed in the northern (Arunta Orogen) and southern (Musgrave Complex) parts of the basin due to their uplift during Petermann (Ediacaran-Early Cambrian) and Alice Springs (Paleozoic) orogenies. Northward, the exposed basement complex consists of deformed meta-sedimentary and meta-igneous felsic and intermediate rocks, whereas the southern basement is constituted by high-grade metamorphic fedspathic gneiss and intrusive igneous bodies (Jackson et al., 1984; Marshall et al., 2007; Carr et al., 2016). The Amadeus Basin extended westwards where an NNE-striking shallow ridge of crystalline basement was emplaced during the Late Paleozoic orogeny. Prior to latest Paleozoic, sediment accumulation in Amadeus Basin was linked to a continuous deposition southward (Powell et al., 1994). The sedimentary basin-fill was initiated during the Early Neoproterozoic and the pre-salt

sediments comprise a quartzite-rich siliciclastic package of the Dean/Heavitree Formation which is exposed along the northern margins of the basin (Fig.2; Walter et al., 1995).

The Petermann and Alice Springs orogenies controlled sedimentation and distribution of the basin-fill sedimentary successions in Amadeus Basin. During Petermann Orogeny (~550-535 Ma), parts of the Amadeus Basin was either uplifted, eroded or locally metamorphosed along the southern margin with synchronous deposition of thick siliciclastic materials that were sourced from the uplifted parts (Bagas et al., 1996; Haines et al., 2015). The Petermann uplift phase was likely accompanied by salt movements; however, the irregular patterns of the folds reveal that the salt-related structures were evolved as earlier growth features prior to their reactivation during the orogenic uplift. Alice Springs orogeny (~400 Ma) largely affected the northeastern part of the basin and was accompanied by a contemporaneous deposition of synorogenic sedimentary facies that are preferentially localized in the northern and northeastern parts of the basin.

The Heavitree Formation comprises quartz-rich sandstones overlying unconformably the basement complex. The sandstones are intercalated with siltstones and conglomerate, and are mostly of fluvial to shallow marine origin. The Heavitree sandstones are followed by carbonates and fine-grained siliciclastic and evaporites of Bitter Springs Group. The Heavitree-Bitter Springs contact is only conformable in the eastern parts of the basin. In the northern parts, the Bitter Springs Group comprises, from bottom to top, the Gillen, Loves Creek and Johnny Creek formations (Fig. 2). The Gillen Formation consists of thick evaporite deposits (halite, gypsum) interbedded with dolomite, shale and siltstone. The Loves Creek Formation is made of stromatolitic dolomite facies unconformably overlying the Gillen facies and conformably followed by the lacustrine red dolomitic and evaporitic mudstone of the Johnys Creek Formation. The post-Bitter Springs stratigraphy comprises thick mixed carbonate and siliciclastic sediments resting unconformably above the evaporitic mudstone and dolomite of the Johnys Creek Formation. The Amadeus Basin contains thick, well-developed Paleozoic sedimentary successions (mostly shales, siltstone and minor sand interbeds) except in

the western regions where the Paleozoic sediments are comparatively thinner (Marshall, 2003; Haines et al., 2010; Normington et al., 2015).

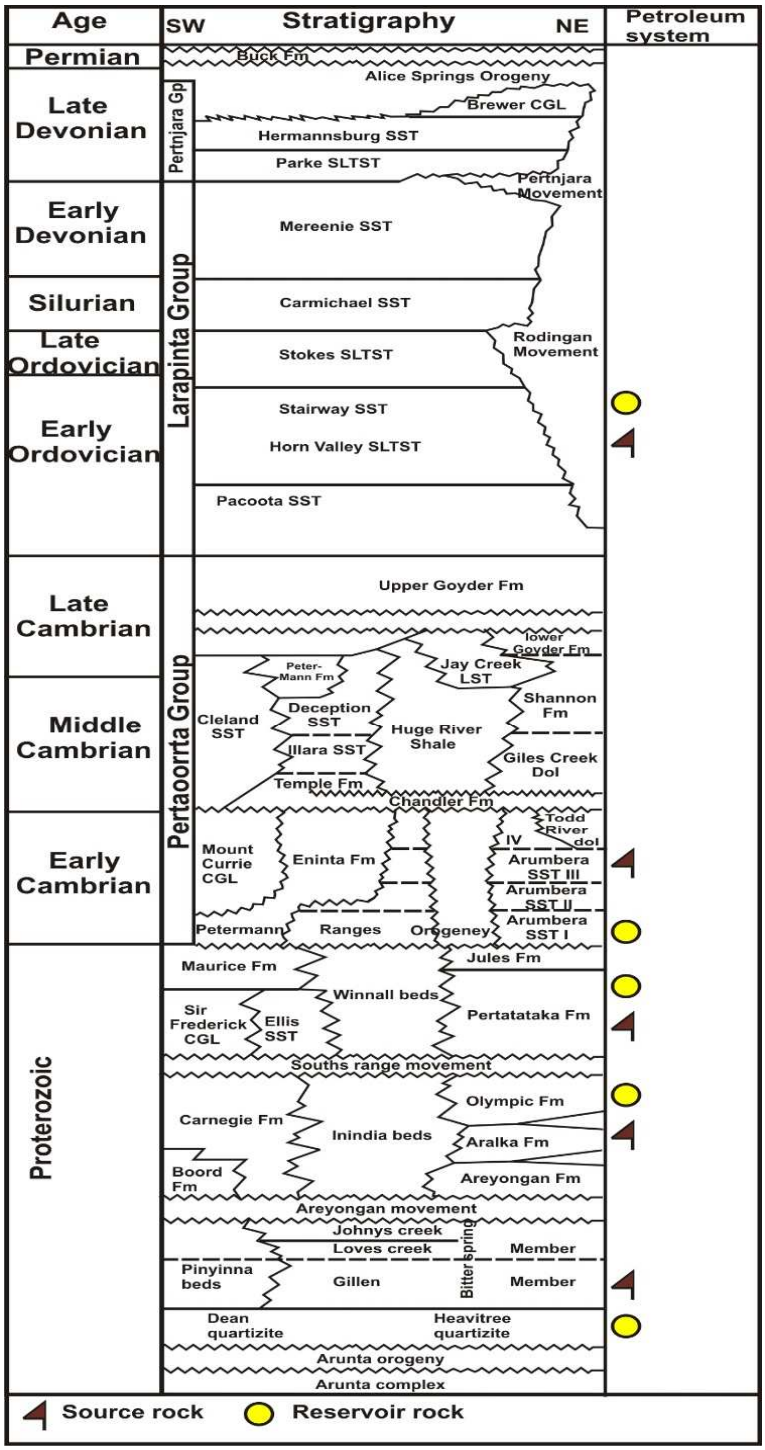

Fig. 2. Generalized composite stratigraphic column for the Amadeus Basin illustrating the tectono-stratigraphic framework of the basin and the possible source rocks and reservoir intervals (Marshall, 2004).

Hydrocarbon exploration to date in the Amadeus Basin focused on the Paleozoic successions principally targeting the structural and combined structural-stratigraphic plays in the shallow salt-related structures in the north. The discoveries so far are post-salt and located in the northern part of the basin, however, the subsalt strata are shallower southward and exploration has been started there since the last decade. For the pre-salt petroleum systems, Heavitree Formation presents a potential reservoir that could be sourced from the shale intervals in Bitter Springs Group (Marshall, 2003). The evaporites of Gillen and Loves Creek Formations are likely to be effective cap rock for the gases that may accumulate in Heavitree reservoir.

3. Data and methods

The Australian policy towards the dissemination and sharing of scientific advances allows access to a lot of information directly on the government site of the Department of Geosciences (https://www.ga.gov.au/). The available subsurface dataset utilized in this study includes 2D seismic, wireline logs as well as analytical internal reports.

3.1. Seismic dataset

The subsurface seismic dataset constitutes regional post-stack 2D seismic grid covering an area of approximately 30,000 km^2 in the eastern and central parts of the Amadeus Basin. In addition, local 3D seismic blocks around the studied Magee-1 and Mt Kitty-1 wells have also been utilized in this study (Fig. 1). The seismic data was interpreted using Petrel Schlumberger 2017 software following the standard seismic interpretation scheme of Herron (2011). The seismic data (time) was tied with well logs (depth) using check shots that were available for all the studied wells.

3.2. Wireline logging analysis

A complete set of wireline logs for Magee-1, Mt Kitty-1, and Murphy-1 wells have been interpreted using the Schlumberger Techlog 2017 software. The available well logs include gamma ray (GR), bit size (BS), caliper (Cal), spontaneous potential (SP), shallow and deep resistivity (LLS, LLD), photoelectric factor (PEF), neutron (NPHI) and

density (RHOB). The GR and NPHI logs were corrected for environmental effects such as borehole size, mud weight and salinity. DST data from Magee-1 well was used to drive Rw values which is approximately 0.04 Ωm at 77°C. The cementation exponent "m" was derived using the triple porosity model (Aguilera and Aguilera, 2004). The wireline logging interpretation includes a qualitative and semi-quantitative estimation for the different petrophysical (porosity Phi, permeability K, water saturation S_w) and lithological parameters using the standard logging interpretation technique.

3.3. Source rock evaluation and gas analysis

Available analyses for Total Organic Carbon (TOC) and Rock-Eval pyrolysis carried out by the operators on 12 cutting samples from Upper (2 samples) and Lower Gillen (8 samples) member as well as Inindia Beds (2 samples) in Magee-1 and Murphy-1 wells were utilized in this study (Table 1, Geotech, 1992). At that time, the cuttings were analyzed using Rock-Eval 2 apparatus following the procedure described by Espitalié et al., (1986). The Rock-Eval pyrolysis peaks include S_1, S_2 and S_3 values which respectively reflect the amount of free, pyrolyzed and organically-bound CO_2 hydrocarbons. Additionally, the temperature at S_2 peak (T_{max}) reflects the source rock maturity (Peters and Cassa, 1994). Geochemical gas analyses comprise the measurement of the molecular gas composition and relative abundance of different hydrocarbon and non-hydrocarbon gases using chromatographic separation. The identified hydrocarbon gas phases comprise C_1, C_2+ components whereas the non-hydrocarbon gases constitute N_2, Ar, CO_2, H_2, and He (Table 2).

3.4. Basin modelling procedure

Burial and thermal history models were constructed for Magee-1 well using Schlumberger PetroMod 1D software to simulate the conditions of hydrocarbon generation and expulsion. The input data for the models comprises a detailed stratigraphic information, thermal boundary conditions, as well as the present-day thermal maturity values. The thermal boundary conditions include the sediment-water interface temperature (SWIT) and the basal heat flow (HF). The paleowater depth (PWD) was determined based on the depositional environment of the sediments. This is an important parameter to define the thermal boundary condition (SWIT). The surface

temperature trends have been synthesized for Magee-1 well in southern Australia (24°S) using the time-latitude diagrams (Wygrala, 1989). The lower thermal boundary condition, paleo heat flow (HF, values in mW/m^2) values were calculated using the known plate tectonic framework and crustal evolution models (Fig. 3; Allen and Allen, 1990). The basal heat flow values follow a general trend reporting a maximum value of 113 mW/m^2 during the main rifting phase of Areyonga, reducing progressively during the compressional tectonic phases of Petemann, Bloodwood, and Rodingan movement and finally reached to 50 mW/m^2 in the present-day (Fig. 3).

Fig. 3. The thermal boundary condition assessment for Magee-1 well including: (top) the paleowater depth (PWD, in meter) and (middle) the sediment-water interface temperature (SWIT, in °C), and (bottom) the paleo-heat flow (HF, in mW/m^2). The basal heat flow values were specified for each geologic event using the present-day analogs and extrapolated through time (Allen and Allen, 1990).

The simulation results were calibrated using equivalent vitrinite reflectance data (VRE) deduced from the measured Rock-Eval T_{max} values (Fig. 4). The calculated vitrinite reflectance from temperature histories was carried out using the EASY-%R_o algorithm of Sweeney and Burnham (1990). The predefined kinetic model_TII(B) of Pepper Corvi (1995) was designated based on the source rock type and depositional environment. The timing of hydrocarbon expulsion was deduced considering that 20%

of the porous volume of source rocks should be filled by hydrocarbons prior to the expulsion onset (Ungerer, 1990). The assigned initial TOC and HI (TOC_o, HI_o) were calculated from the measured TOC and HI following the procedure described by (Peters et al., 2005).

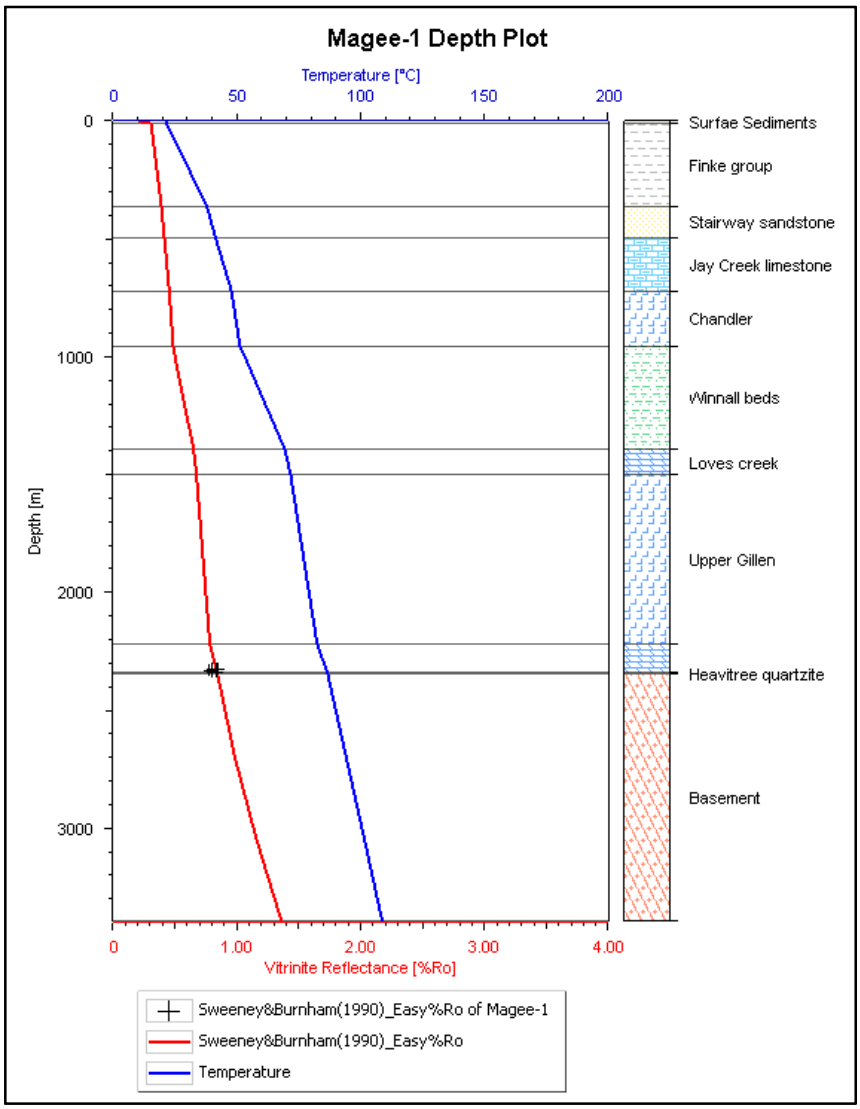

Fig. 4. The depth plot of the present-day thermal maturity of the Magee-1 well calibrated with the theoretically calculated equivalent vitrinite reflectance (VRE) values.

3.5 Petrography

Three thin sections were prepared from the cutting and SWC samples retrieved from the 7 m thick Heavitree sandstones in Magee-1 well (Geotech, 1992). The cuttings were impregnated with araldite and blue dye to facilitate the visualization of pore spaces and

quantification of porosity. Additionally, the thin sections were stained with sodium cobaltinitrite to identify feldspars.

4. Results

4.1. Surface emanations

Several sub-circular depressions (SCD) have been recognized from the satellite images in the study area. The observed SCD are similar to those reported for surficial H_2 emitting structures, the so-called fairy circles, as described in south and west Australia (Moretti et al., 2021a; Frery et al., 2021, Geymond et al., 2022). High densities of scattered, slightly elongated SCD are observed near the Amadeus Lake (Fig. 5). The diameter of the SCD structures varies from several tens to hundreds of meters and most of them have diameters greater than 400 m. The large SCD often display concave-up elevation profiles with smooth topography, whereas the small depressions (< 200 m diameter) have sharp, concave-up and irregular elevation profiles.

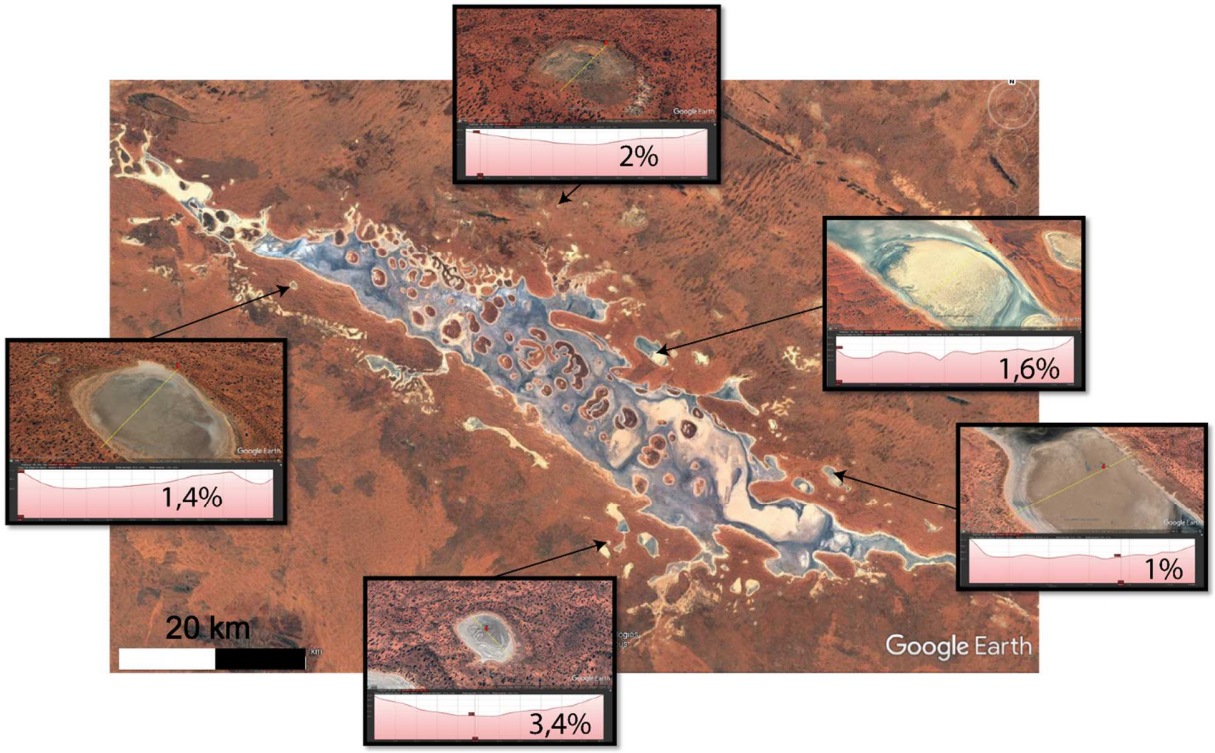

Fig. 5. Google Earth photographs illustrating occurrence of several aligned Sub Circular Depressions in Amadeus Basin with variable depth/equivalent diameter ratios highlighted in red.

The depressions also contain some local highs usually localized in the center. The depth/equivalent diameter ratio of the SCD ranges from 1% to more than 3% (Fig. 5). These values are very similar to the ones reported in other parts of Australia and in the areas where H_2 emitting structures have been mapped (Moretti et al., 2021b, Geymond et al., 2022). Moreover, a trend of SCD is observed to the south of the Amadeus Lake. They are aligned in NW-SE direction parallel to the faults associated with Petermann Orogeny (Fig. 6) suggesting a possible gas leakage along these faults similar to that reported elsewhere such as in Russia (Larin et al., 2015).

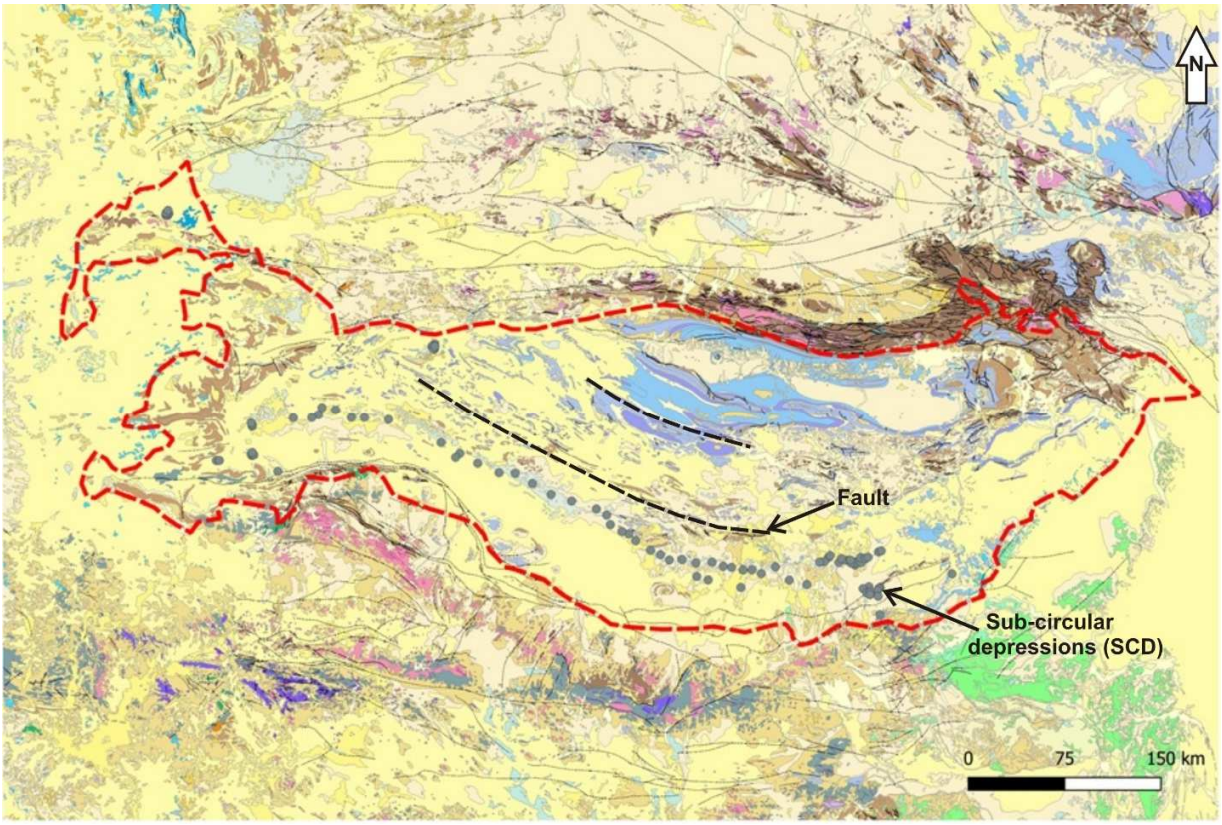

Fig. 6. Map illustrating the distribution of the sub-circular depressions (SCD) in the southern part of Amadeus Basin, grey dots. The depressions are aligned parallel to the master NW-SE trending fault trends affecting the basin. One may note the highest density of the SCD eastward near the wells that proven the presence of H_2.

371

372

373 ### 4.2. Seismic interpretation

374 The interpreted 2D seismic profiles delineate the complex structural elements that
375 influenced the stratigraphic architecture of the study region. The seismic profiles
376 illustrate chaotic and reflection free seismic reflections interpreted as crystalline
377 basement that are often dissected by large deep-sated faults (Figs. 7A, B and 8). The
378 basement is picked at relatively shallow depths (< 2000 millisecond two-way time ms
379 TWT), however several basement highs (< - 1700 ms TWT) are locally observed. The
380 basement top is defined by irregular, undulated non-conformity surface. Thin-skinned
381 deformation features probably associated with the Petermann Orogeny with major faults
382 detached within the basement and the overlying pre-salt and salt layers are identified as
383 the most prominent structural elements. The faults are mainly dipping westward with
384 displacements up to 300 ms TWT at the top of the Gillen Formation. The basement
385 faults were likely reactivated during Petermann Orogeny resulting in a formation of
386 multiple local antiforms associated with inverted basement blocks (Fig. 8).

387 The pre-salt Heavitree Formation is represented by discontinuous high amplitude
388 and reflectivity seismic reflections locally onlap the non-conformity surface topping the
389 basement (Fig. 7A, B). The Heavitree reflections are localized in the basement lows and
390 depressions adjacent to the deep faults (Fig. 7A), where they attained a maximum
391 thickness of less than 100 ms TWT. The basement is relatively deeper in the
392 southwestern part of the study area where its top is picked at more than - 2500 ms TWT
393 (Fig. 9A).

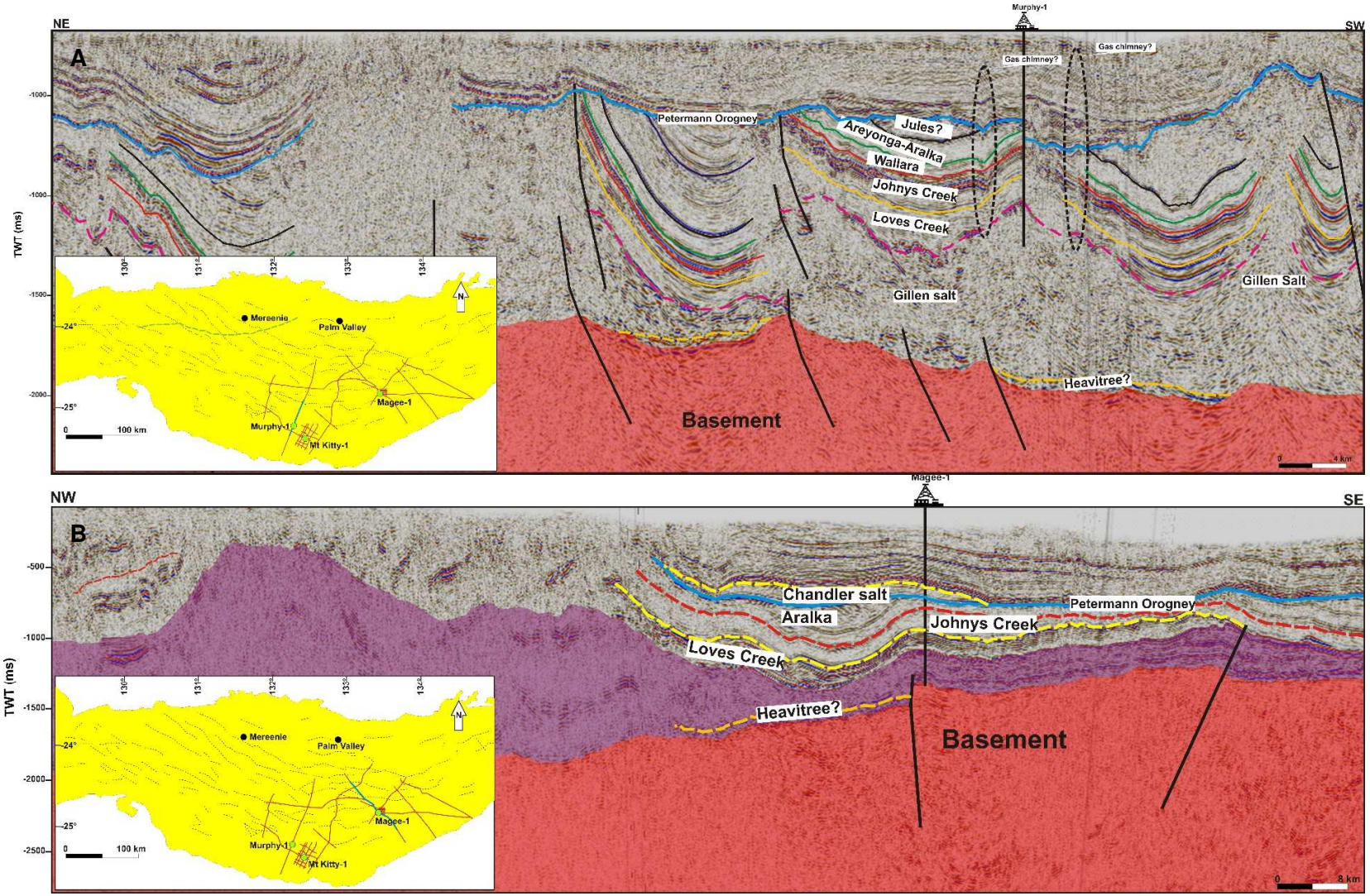

Fig. 7. Interpreted 2D seismic profiles showing the distribution of the different stratigraphic horizons and the major structural elements. Seismic location: green line on the map.

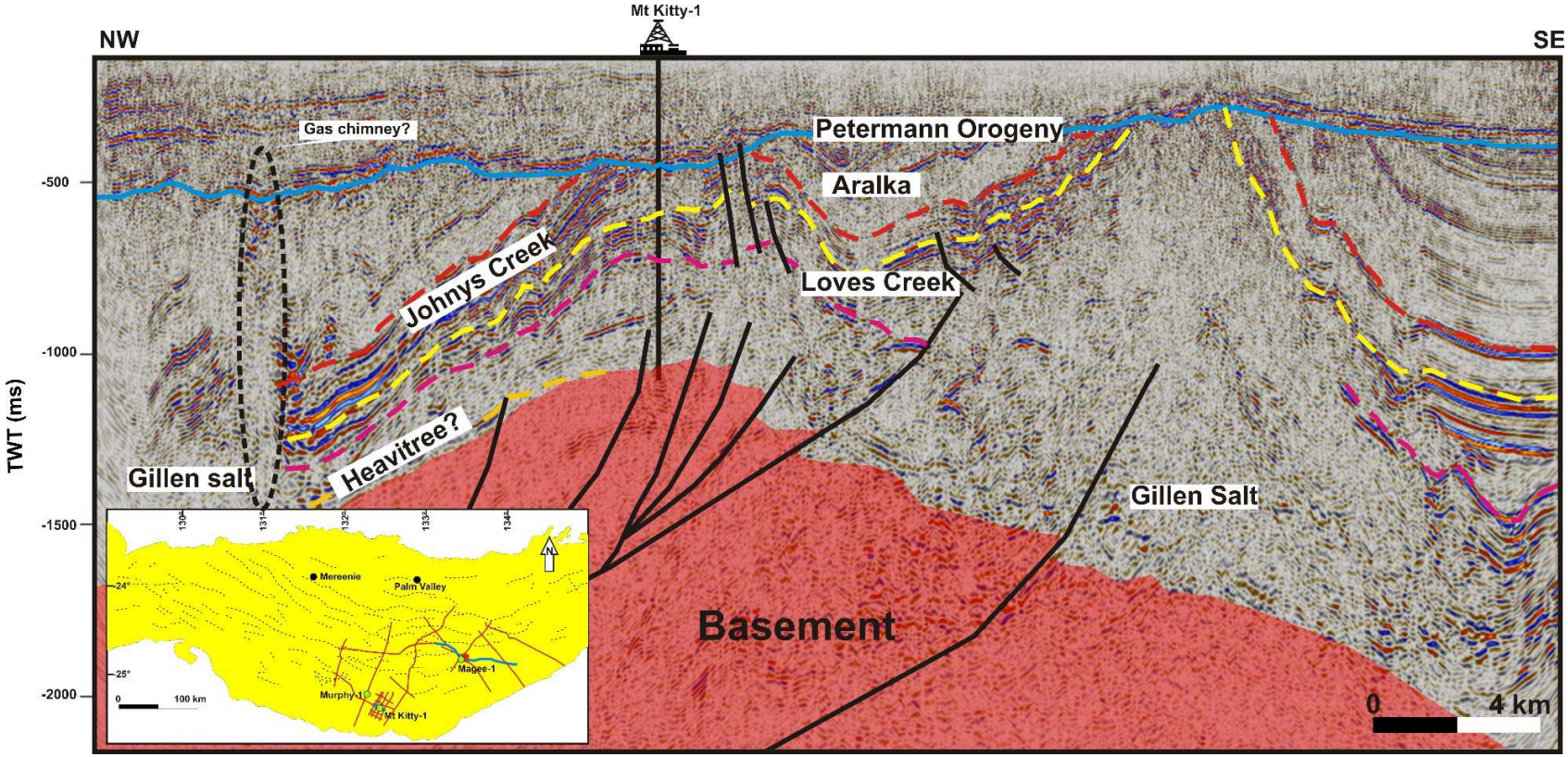

Fig. 8. Interpreted 2D seismic profile illustrating the main fault trends in Mt Kitty structure.

The Gillen salt is characterized by very low amplitude, transparent to semi-transparent chaotic reflections (Figs. 7A, B and 8). Lower Gillen reflections are less chaotic with moderate amplitude and reflectivity, locally displaying discrete patches that are localized in the basement highs (carbonate build-ups?). In some parts such as in Magee-1 well area, these patches are followed by thin (~ 15 ms TWT), high amplitude horizontal, continuous reflections interpreted as halite layers. The top of the Gillen salt is picked at variable depths in the study area, however, it is relatively shallower and thicker in the west than in the east (Fig. 9B). Loves Creek reflections are semi-transparent and display low to moderate amplitude and reflectivity. They grade upward into the parallel, high amplitude and reflectivity reflections of the Johnys Creek Formation. The seismic reflections of the Bitter Springs Group are terminated against Petermann unconformity characterized by high amplitude, continuous, and irregular reflector erosionally-truncating the pre-Petermann reflections. The Petermann unconformity is picked at greater depths in the eastern part of the study area (~ -1000 ms TWT, Fig. 10A). The Gillen salt has been mobilized possibly during the Petermann Orogeny, and therefore its thickness varies greatly in the study region (Fig. 10B). Reactivation of the basement faults during the Petermann Orogeny is more prominent in the western part of the study area resulting in the inversion of the basement blocks associated with formation of flower-like structures (Fig. 8).

Several forms of chaotic and disordered vertical disturbances have been observed on seismic and were interpreted as gas escape structures (gas chimneys). They are represented by vertically-aligned columnar features associated with an abrupt decrease in the reflection amplitude and continuity (Figs. 7A, B and 8). The observed gas chimneys often traced vertically from the basement to the Petermann unconformity where they often disturb the overlying layers. They range in size on the horizontal scale from several few tens of meters up to 500 m (Fig. 11). None of these features are associated with pockmarks that often reflect entrapment of the migrated gases. In this kind of salt-rich basin, some of these disturbances in seismic reflections may also be induced from the mobilization of salt forming salt scars.

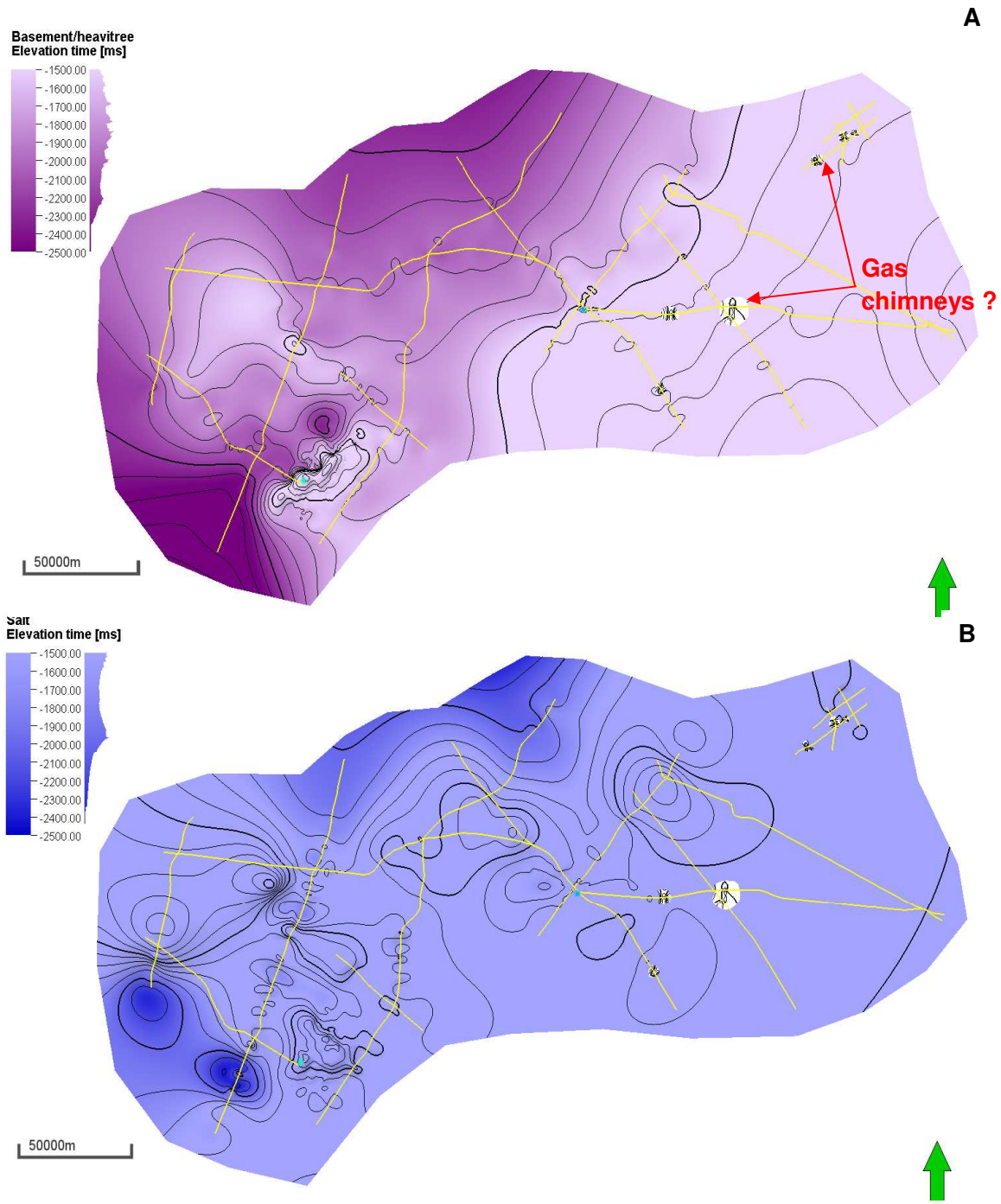

Fig. 9. A) Depth contour maps at the top of Heavitree Formation/basement and Gillen Salt (B) illustrating relative deepening in the southwestern part of the study area. Projected gas chimneys often occur in the eastern part where the basement and salt are relatively shallow.

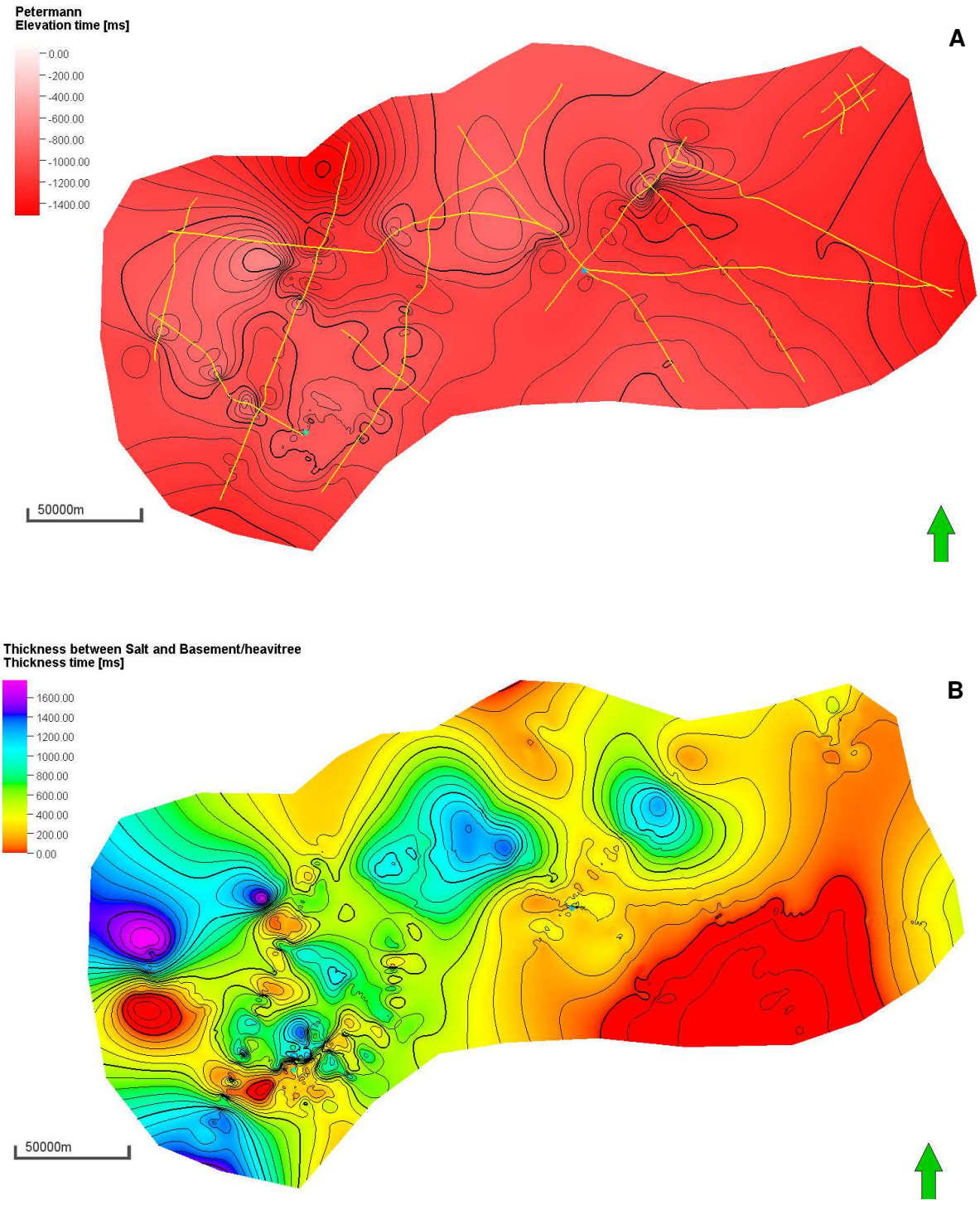

Fig. 10. A) Depth contour maps at the top of Petermann unconformity; B) Thickness map showing variations in salt distribution and its thinning in the eastern part of the study area.

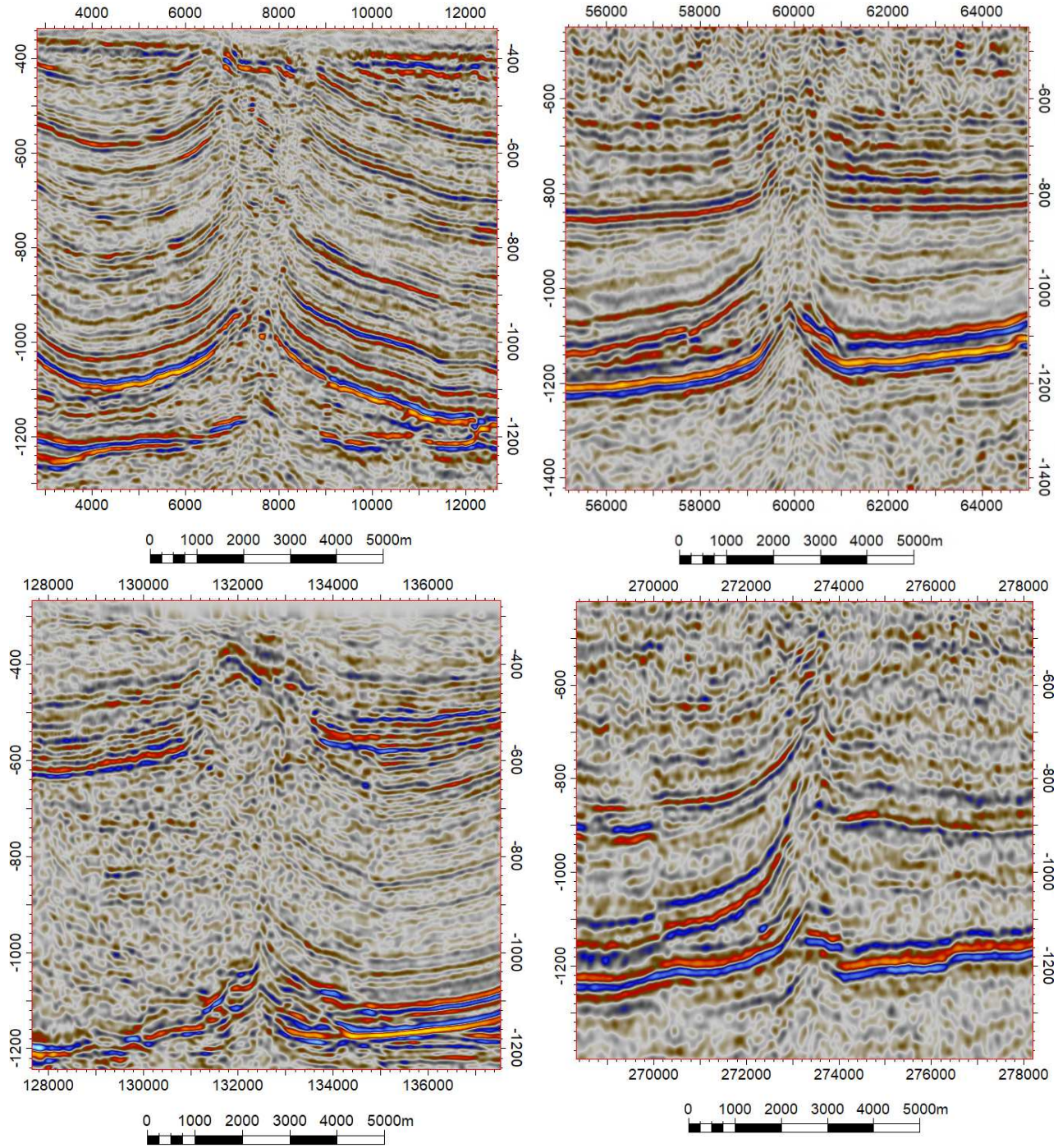

Fig. 11. Local vertical disturbances in the seismic reflections possibly reflect occurrence of gas chimneys and/or salt scars.

4.3. Lithologic composition of Heavitree reservoir

The Heavitree Formation consists mainly of quartzose sandstone with a framework composition dominated by quartz, feldspars and subordinate lithic fragments (Fig. 12A, B). The framework components are medium to coarse grained, poorly to moderately sorted and sub-rounded to sub-angular. The feldspars are fresh to partly altered and are mainly represented by K-feldspars (Av. 8%) with minor plagioclase (Av. 1%). The lithic fragments (Av. 5.5%) are mainly sedimentary (claystone) with minor igneous and metamorphic fragments. The sandstones have an average composition of $Q_{77}F_{15}L_{8}$, and are therefore classified as quartz to subfeldspathic arenite (Fig. 12C). The framework components are tightly-compacted and display sutured and concavo-convex grain contacts (Fig. 12B). Moreover, the feldspars are partly dissolved forming secondary pore spaces. Quartz overgrowths are often associated with the sutured grain contacts. Authigenic clays are observed on the altered feldspars.

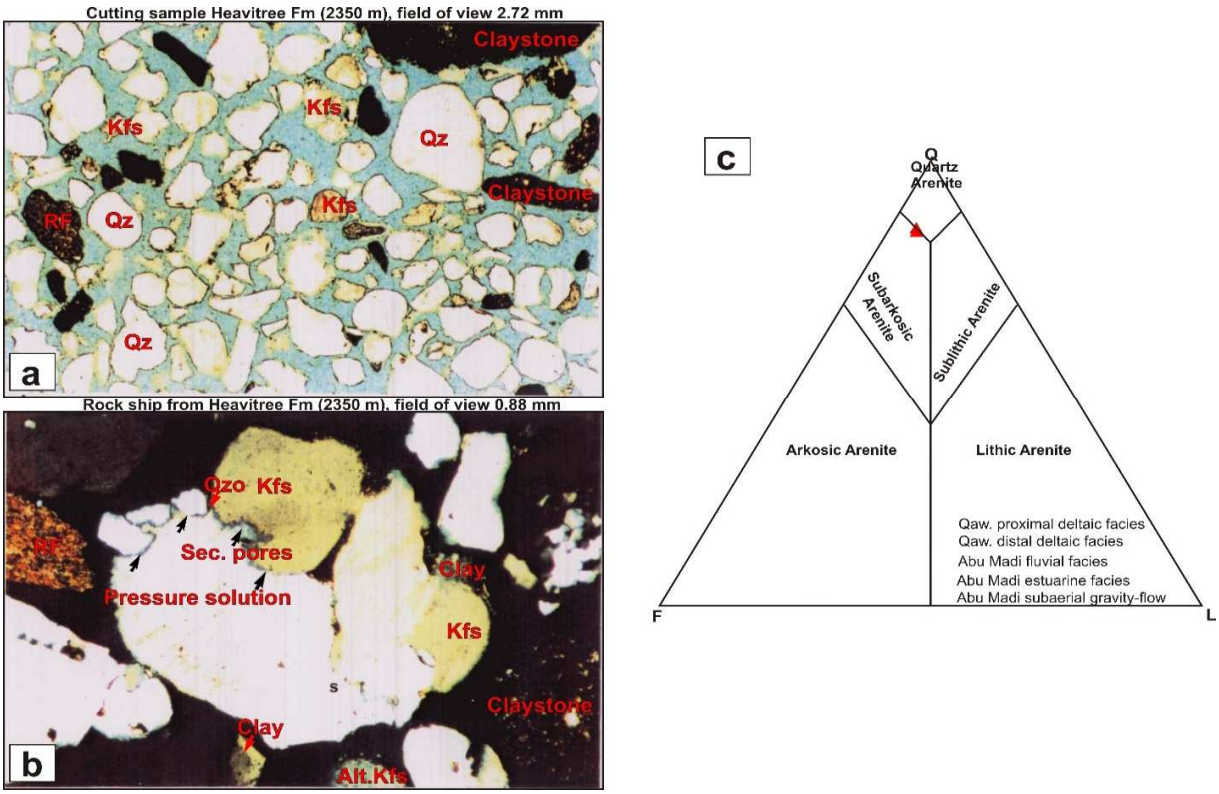

Fig. 12. Thin section microphotographs showing the mineralogical composition of Heavitree Formation (Amdel core services, 1993): A) cutting sample in PPL, B) Rock sample in XPL, C) QFL modal composition of the studied Heavitree sandstone samples (Blatt and Tracy, 1996). Mineral symbols: quartz (Qz), K-feldsprs (Kfs), rock fragment (RF), quartz overgrowth (Qzo).

4.4. Wireline log analysis

Interpretation of wireline logs aids in the identification of different petrophysical parameters that determine the reservoir potential of the Neoproterozoic succession in the study area. In Magee-1 well, porous gas-bearing intervals are scarce and often localize above the basement at the base of the Gillen salt (Fig. 13). Heavitree pay (6 m thick) is characterized by a blocky gamma ray pattern with very low values (20-30 API). The Heavitree pay zone has an average clay volume of 17%, however, most of the clay materials are present in structural forms (claystone fragments, Fig. 12A) and therefore they do not adversely impact the porosity values (Av. 13%). The pay zone sandstones also display low water saturation values (Av. 34%) and a notable neutron-density crossover typifying the presence of trapped gas. Another porous, gas-bearing interval is observed above the Lower Gillen succession. This interval consists of approximately 20 m thick halite layers characterized by very low gamma ray values (< 10 API). This halite interval is also traced in Murphy-1 well at the base of Gillen Salt (Fig. 14). The halite beds have very high porosity (Av. 23%) and very low clay volume (< 5%) values.

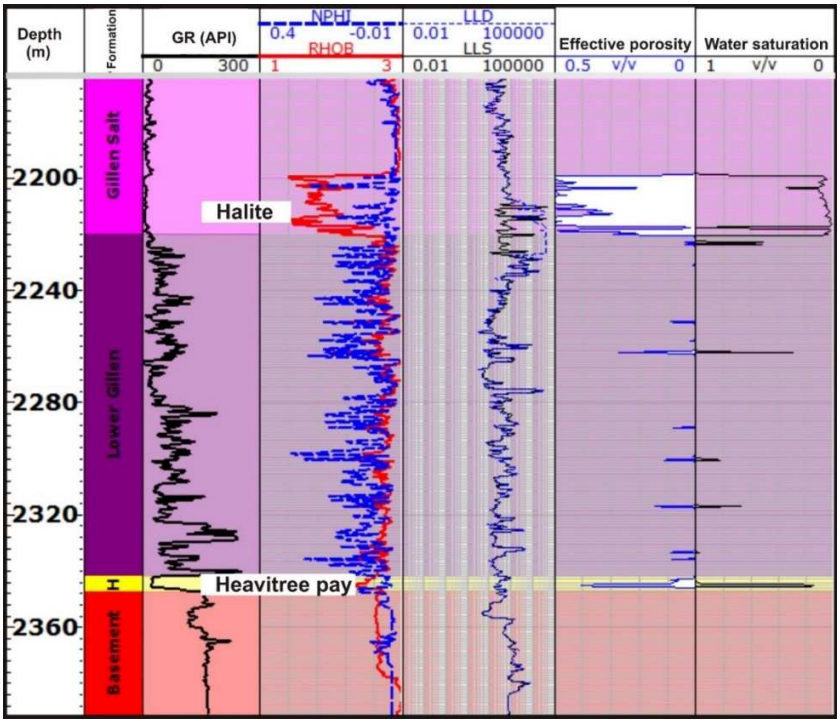

Fig. 13. Vertical distribution of the different wireline logs data including the calculated values of effective porosity and water saturation in Magee-1 well.

The abnormally high porosity of the halite possibly reflects a gas entrapment in the pore spaces during halite crystallization (Blamey et al., 2016). The elevated resistivity values (> 200 ohm.m) and the prominent neutron-density crossover coupled with the very low water saturation values (Av. 9%) are evidence for gas entrapment in the halite crystal lattice. In Mt Kitty-1 well, porous intervals are locally observed in the basement rocks where the effective porosity values are up to 13% with an average value of 4% (Fig. 15). The basement contains several fracture zones characterized by anomalously high resistivity values with a notable separation between shallow and deep resistivity curves characteristics for gas-filled fracture network (Sw < 50%). The fracture zones also display very low formation matrix density and high neutron values typifying a possible invasion of mud filtrate.

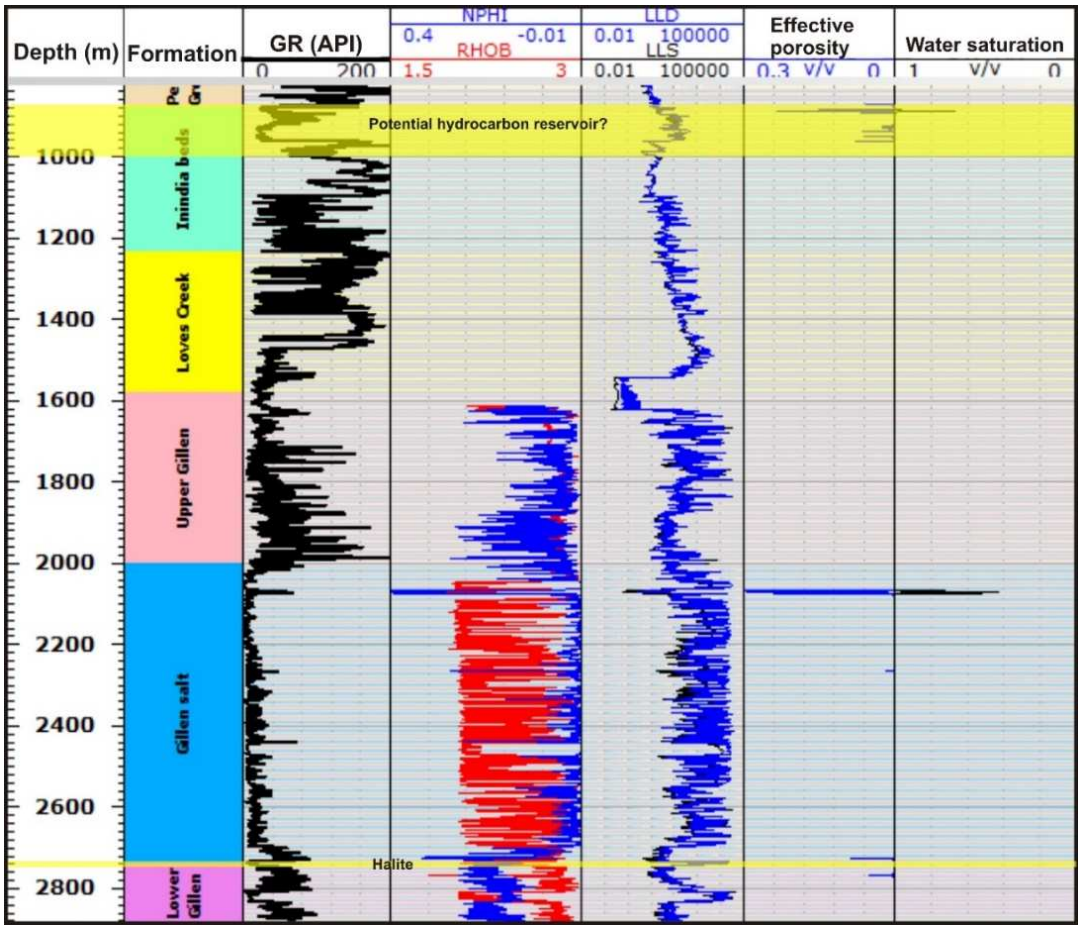

Fig. 14. Vertical distribution of the different wireline logs and calculated values of effective porosity and water saturation showing some potential above salt reservoir intervals in Murphy-1 well.

4.5. Source rock characteristics

The investigated shales from Lower and Upper Gillen have low TOC values < 1 wt%. Those of Lower Gillen have slightly higher TOC values (Av. 0.57 wt%) than the Upper Gillen samples (Av. 0.50 wt%). Elevated TOC values (however lower than 2 wt%) are observed in the shales of Inindia Beds. Most of the TOC content is attributed to the residual carbon (RC), whereas the pyrolyzed carbon (PC) values are very low (Table 1). The Rock-Eval S_1 values are low in the Lower Gillen and Inindia Beds shales (Av. 0.1 mg HC/rock) and are comparatively higher in the Upper Gillen shale samples (Av. 1.5 mg HC/rock). Rock-Eval S_2 values are lower than 1 in all the studied rocks. Similar to S_2, the Rock-Eval S_3 values are less than 1 with values ranging from 0.04 to 0.60. Additionally, the T_{max} values vary in a wide range in lower and Upper Gillen samples (393-445°C and 350-393°C, respectively), and they range between 433°C and 435°C in

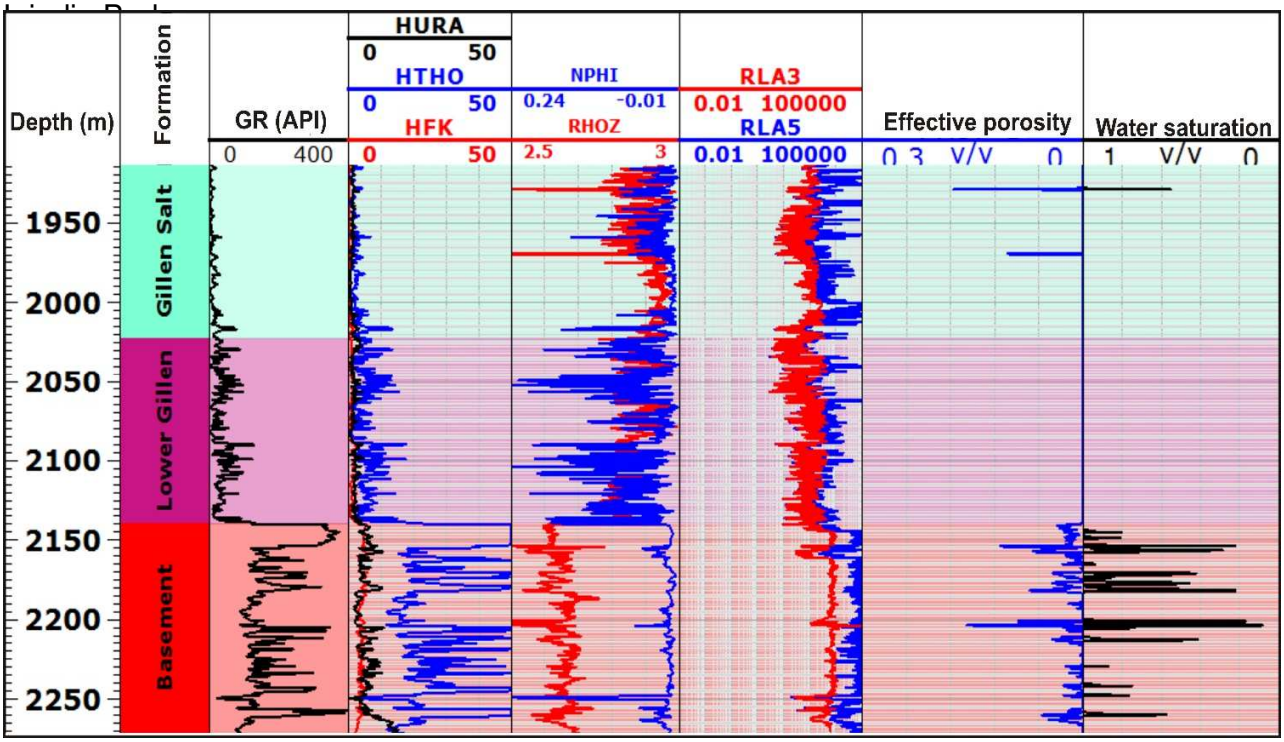

Fig. 15. Vertical distribution of the different wireline logs showing potential reservoir intervals only in the sub-salt basement of Mt Kitty-1 well.

The production index (PI) is high in the Upper Gillen samples with a maximum value of 0.77, while it is relatively lower (< 0.4) in the Lower Gillen and Inindia beds samples (Table 1). The generative potential (GP) is less than 1 except in one sample of the Upper Gillen. The hydrogen index (HI) values are very low in Lower Gillen and Inindia Beds shales (31-60 and 17-21 mg HC/g TOC, respectively) and are higher in the Upper Gillen with values ranging between 90 and 159 mg HC/g TOC. Similarly, the oxygen index (OI) values are very low in all the studied samples with values less than 50 and 5 mg CO_2/g TOC in the Lower Gillen and Inindia Beds, respectively, whilst elevated OI values are only observed in the Upper Gillen samples (Table 1).

4.6. Hydrocarbon and non-hydrocarbon gas analysis

The Magee-1 well gases consist mainly of N_2 and CH_4 comprising approximately 75% of the whole gas composition. Other gas phases comprise He (6.20%) with subordinate contents of C_2 and C_{2+} components (Table 1). The Magee-1 gas is characterized by higher IC_5/nC_5 than IC_4/nC_4, and a dryness coefficient (DC) value of 0.80. Mt Kitty-1 gases are characterized by elevated N_2 contents that range from 61% to approximately 100%. They contain variable contents of CH_4 (0.04-13.14%) with subordinate quantities of He (0-9%) and H_2 (0-11.4%). C_{2+} phases are also significant in Mt Kitty-1 gas samples where the DC values are often less than 0.75. Notably, Mt Kitty-1 gases display much greater IC_5/nC_5 relative to IC_4/nC_4 (Table 1). In Murphy-1 gas samples, the hydrocarbon gases mostly constitute CH_4 with variable contents of C_{2+} components. Murphy-1 gases also display a wide range of DC values between 0.79-0.90 and show relatively elevated IC_4/nC_4 than IC_5/nC_5 values.

669

670 ### 4.7. Burial model

671 The burial model of Magee-1 well highlights five major tectonic phases that have
672 controlled the sediment distribution and architecture in the study region. These tectonic
673 events comprise: the earliest Areyonga rifting phase that is followed by four successive
674 younger compressional events. These are the Petemann, Bloodwood, Rodingan and
675 Alice Springs oroginies. The heat flow corresponding to these tectonic phases are
676 assigned as follows: 113, 75, 72, 70, and 65 mW/m^2, respectively. These tectonic
677 phases likely controlled the thermal maturity of the Lower Gillen organic-rich shales
678 (Fig. 16). The pre-rift sediments were subjected to a moderate subsidence which
679 created an accommodation space for the accumulation of the thick salt layers (Gillen
680 salt) and the massive white dolomite (Loves Creek) above the Lower Gillen sediments.
681 The syn-rift phase (Areyonga rifting) was characterized by a lithospheric streching
682 coupled with elevated levels of heat flux. Contemporaneous to the post-rift thermal
683 subsidence (Cambrian-Ordovician), very thick sedimentary successions of post-rift
684 clastic facies were deposited. The post-rift thermal subsidence has been ended with the
685 onset of the successive compressive phases (Petemann, Bloodwood, Rodingan and
686 Alice Springs oroginies) during which the subsidence rate has significanlty decreased
687 (Fig. 16). The top of oil window was reached at relatively shallow depths (~ 1350 m).
688 Additionally, the expulsion onset and the gas window maturity were observed at greater
689 depths (~ 2338 m) and higher temperatures (~ 117 °C, Fig. 17) compared to the oil
690 window.

691

692

693

694

695

696

697

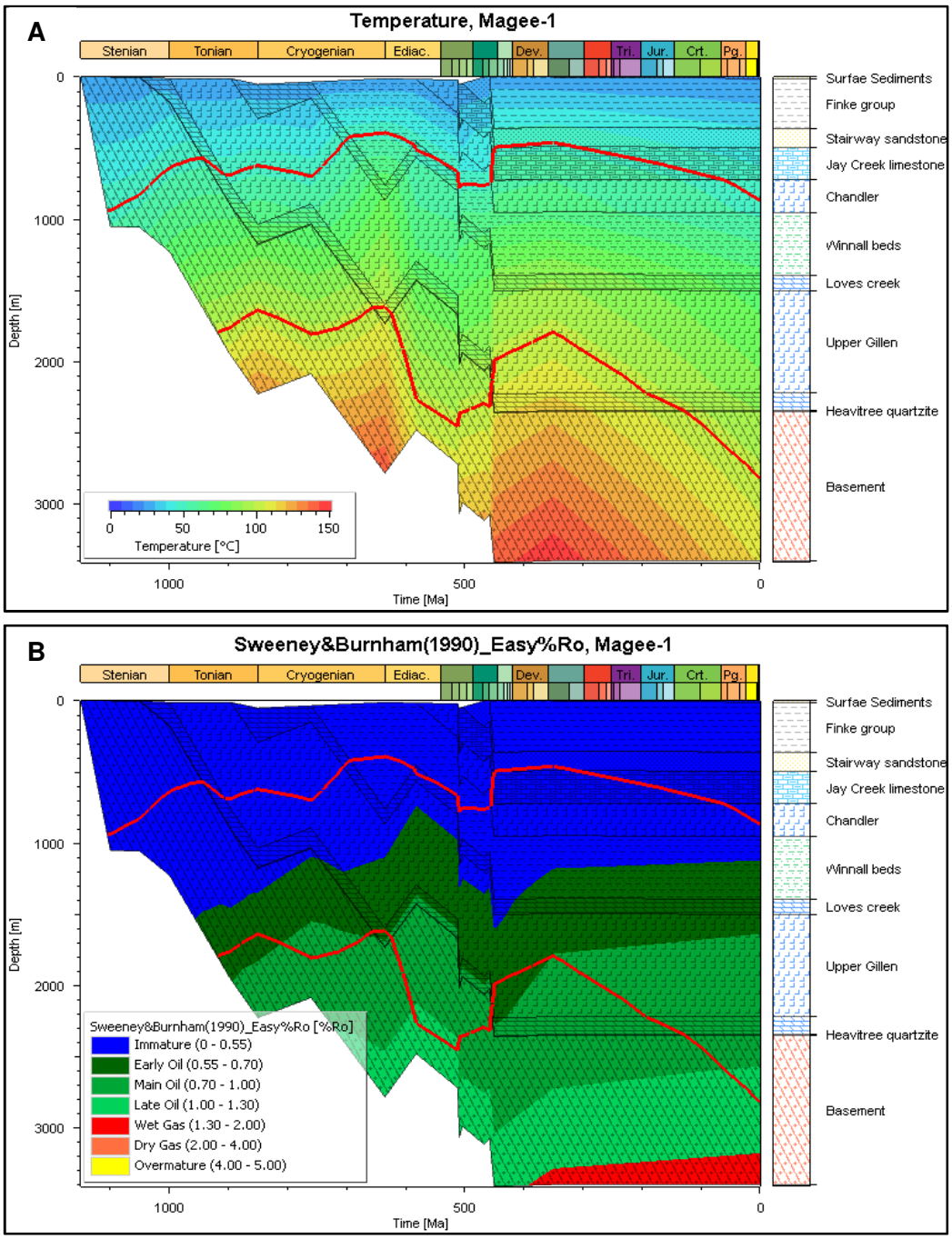

Fig. 16. Illustrative burial models for the sedimentary succession in Magee-1 well. The temperature overlay (A) is added to demonstrate the thermal history. The simulated vitrinite reflectance maturity overlay (B) was deduced using the EASY%_Ro algorithm

(Sweeney and Burnham, 1990) as a function of time and space. The red lines represents the temperature intervals for 50, and 100°C.

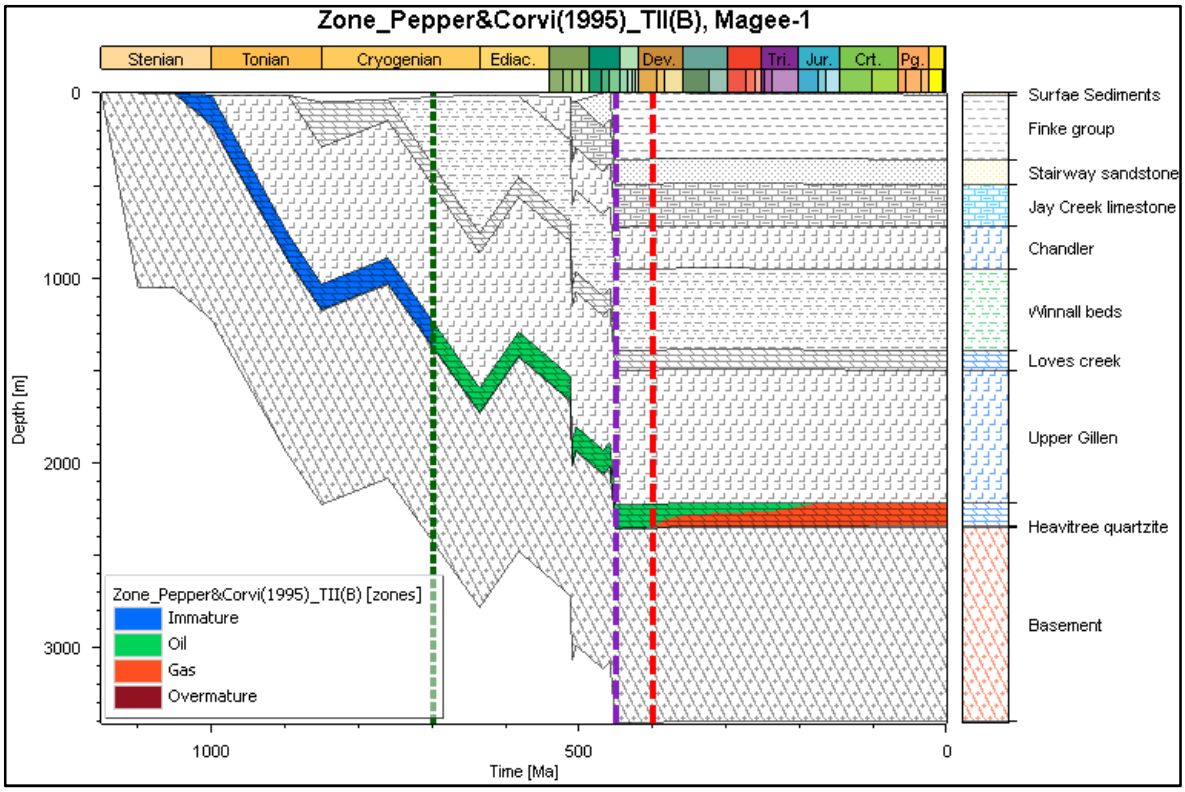

Fig. 17. The burial history chart of Magee-1 well with the hydrocarbon generation zone overlay according to TII-B kinetic model of Pepper and Corvi (1995) through geologic time. The vertical colored dashed lines represent the onset of oil generation at ~ 700 Ma (green dashed line), the vertical purple dashed line represents the expulsion onset at 448 Ma and the red dashed line points to the gas generation window at 400 Ma.

5. Discussion

5.1. Hydrocarbon gas origin, generation and expulsion

The TOC and Rock-Eval pyrolysis results are frequently used to investigate and assess the capability of the organic-rich sediments to generate thermogenic hydrocarbons (Peters, 1986; Peters and Cassa, 1994, Leila and Moscariello, 2017). Based on the measured TOC values, Lower and Upper Gillen shales contain fair contents of organic matter, whereas the samples of Inindia Beds are richer in the organic content. However, the Rock-Eval S_2 values are below 0.8 that is often

considered as a lower limit to interpret the values in terms of generation potentiality, especially the T_{max} as valid for maturity assessment. The measured S_2 values in studied shales reflect their current poor potentiality to generate hydrocarbons upon thermal cracking of the kerogen. The poor S_2 values in all the shale samples are consistent with their depleted contents of pyrolyzed carbon (Pc), however, most of these samples may have had much higher initial TOC contents than that currently preserved. Based on measured present-day TOC, the initial TOC values were deduced following theoretical calculations proposed by Peters et al. (2005) (Table 1). The maximum initial TOC and HI values were theoretically deduced as 1.3 % and 500 mg HC/g TOC, respectively. Accordingly, potential source rock intervals that could have generated hydrocarbon gases are hosted in the Lower Gillen and Inindia Beds (Fig. 18). However, more data are required to better define the source rock in the deepest part in the drainage area of the drilled structures. In addition, no work has been published for such an old, Precambr and in term of interpr depend on equivalen the maturity level.

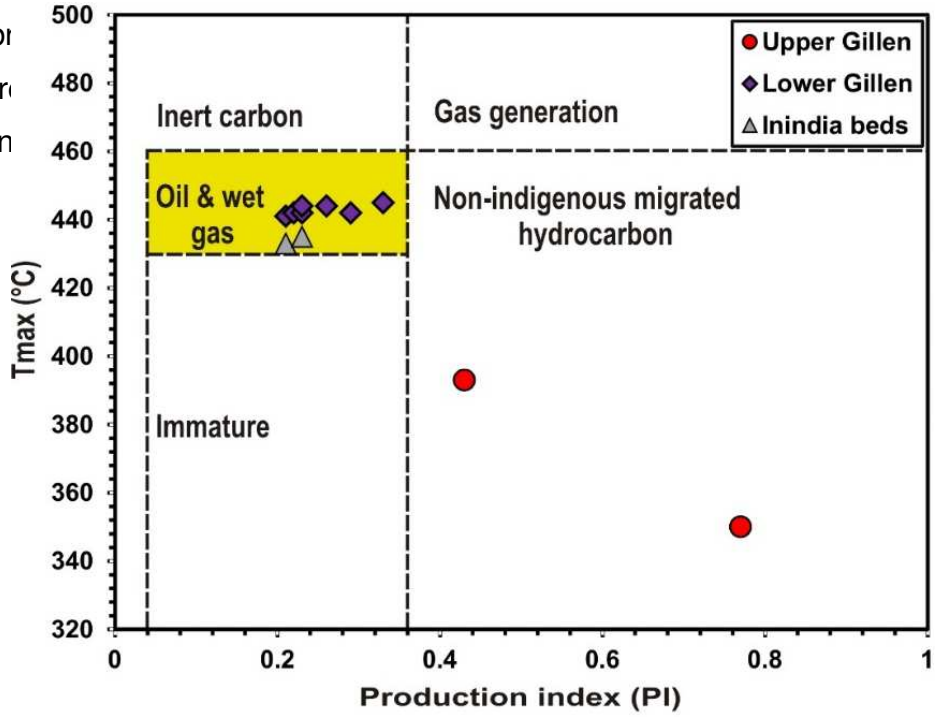

774 **Fig. 18.** Production index (PI) versus Rock-Eval T_{max} plot illustrating the potentiality of
775 some intervals in Lower Gillen and Inindia Beds to generate hydrocarbon gases. The
776 investigated shales of Lower Gillen Formation likely generated most of the hydrocarbon
777 gases in the basin.

778 Dominance of C_2 and C_{2+} gas phases in all the investigated HC gases points to a
779 prominent contribution from thermogenic sources (e.g. Tissot and Welte, 1978; Hunt,
780 1996). Furthermore, the calculated dryness coefficient (DC) values for the HC gases are
781 less than 0.95 which is much lower than those reported for pure biogenic gases (~ 0.99;
782 Radwan et al., 2022), thus confirming a dominant thermogenic origin for the studied HC
783 gases (Table 2). Genesis of hydrocarbon gases via thermogenic cracking of organic-
784 rich kerogen is often associated with generation of wet gas components (DC < 0.9),
785 however, mixing with biogenic gas phases would increase the DC values to more than
786 0.9 (Schoell, 1983; Whiticar, 1999). Accordingly, mixed biogenic and thermogenic
787 hydrocarbon gases are common in Murphy-1 well at different depths, whereas gases
788 collected from the other wells only contain thermogenic hydrocarbon gases. Occurrence
789 of some alkanes and their relative proportion such as iC_4/nC_4 and iC_5/nC_5 often infers
790 on the conditions of HC gas generation from mature kerogens (Wang et al., 2017, Qin
791 et al., 2018). With increasing thermal maturity, the concentration of the less stable
792 isobutane decreases relative to the more stable n-butane (Qin et al., 2018). The good
793 correlation between the dryness coefficient and iC_4/nC_4 (R^2= 0.75) suggests generation
794 of studied HC gases via primary cracking of an organic-rich kerogen at the gas window.
795 The relationship between natural logarithms of C_1/C_2 and C_2/C_3 ratios commonly reflects
796 the mechanism of HC gas generation (primary versus secondary cracking).
797 Hydrocarbon gases generated via secondary cracking of liquid HC phases often display
798 a progressive increase in both C_1/C_2 and C_2/C_3 ratios (Tao et al., 2014). The studied
799 hydrocarbon gases show a slight increase in the natural logarithms of C_1/C_2 and C_2/C_3
800 ratios typifying their generation from primary cracking of a mature kerogen (Fig. 19).
801 This is consistent with our modelling results and the hypothesis of thermogenic cracking
802 of the Lower Gillen organic-rich intervals that have entered the gas window during the
803 earliest Mesozoic.

Burial modeling results point out that the Lower Gillen had reached the gas window about 200 Ma with a simulated present-day temperature of 86°C (Fig. 16). The initial rifting phase (850 Ma to 760 Ma) was characterized by high heat flow value; however, it did not contribute to the HC generation due to the high thermal conductivity of the Upper

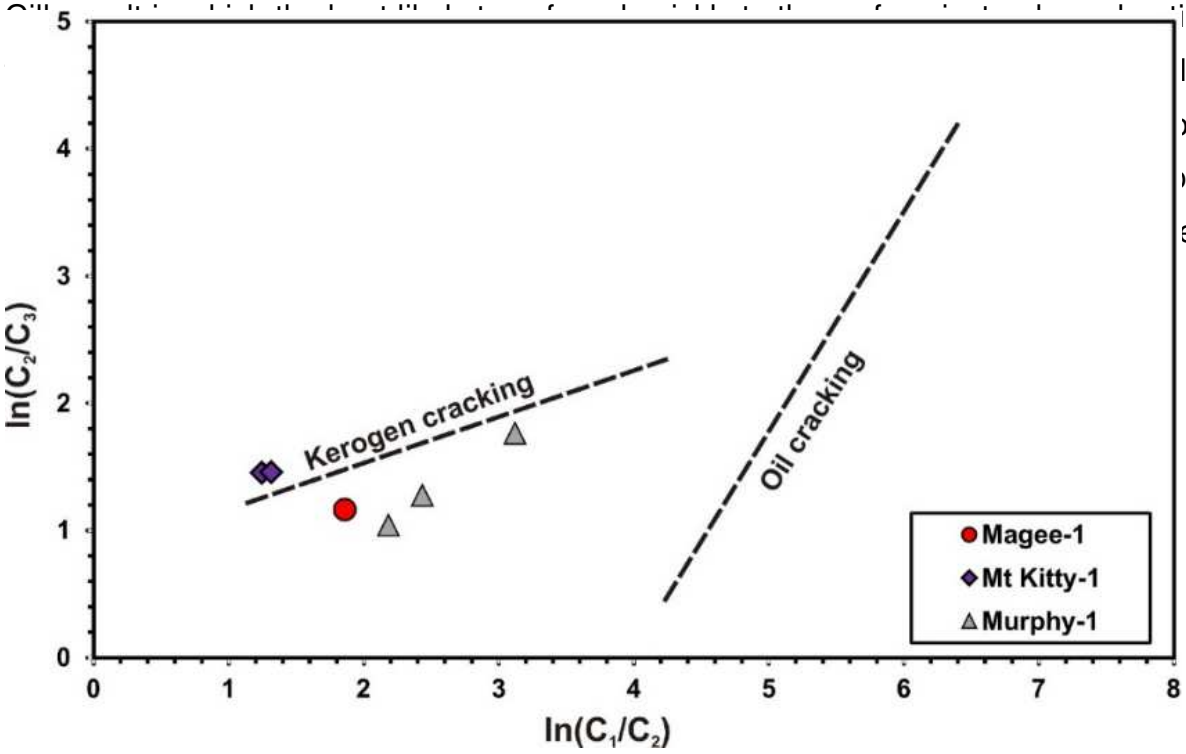

Fig. 19. Plot of ln C_1, C_2 and C_3 values typifying generation of the studied HC gas phases via primary cracking of the kerogen (Tao et al., 2014).

The transition from liquid to gaseous hydrocarbon generation was gradual with a generation phase of wet gases within the oil window. The 1D modeling results elucidated that the gas window occurred at a burial depth of 2340m in Magee-1 well. The first two tectonic events have induced a minimal impact on the hydrocarbon

generation due to the cooling effect of the overlying Gillen salt layers. Despite the fact that the burial temperature did not exceed 110°C and was even constant since the Late Paleozoic, the prolonged exposure to this temperature resulted in a slow maturation of the organic matter and kerogen transformation into hydrocarbons (e.g. Loptain, 1971; Waples, 1980; Wood, 2018). We hypothesize that the kerogen type of the initial organic matter, the interplay between burial temperature, exposure time as well as the cooling effect induced by the Upper Gillen salt control the type and composition of the generated hydrocarbons.

5.2. Origin of H_2 and He

Helium (He) occurrence in the study area with a maximum content of 9% in Mt Kitty-1 well presents one of the highest recorded subsurface concentrations ever recorded on Earth (McInnes et al., 2017, Boreham et al., 2018). Furthermore, the He-rich gases are mixed with a significant concentration of H_2 (~ 11%) as well as wet hydrocarbon gases (C_1/C_2 ~ 3). This unusual gas blend reveals a complex interplay between various gas generation processes in the subsurface. The occurrence of He in the subsurface is often associated with either mantellic or crustal gases as well as the dissolution of atmospheric gases in the groundwater (Poreda et al., 1986; Ni et al., 2014; Moore et al., 2017). Except mantellic gases, all the other sources are associated with an enrichment of ^{4}He relative to ^{3}He. Therefore, a useful tool to discriminate the origin of He-rich gases is the relative proportion of He isotopic composition (R= ^{3}He/^{4}He) relative to that in the air (R_a= 1.4 × 10^{-6}). For example, the He derived from the upper mantle displays average R/R_a values between 2 and 8, whereas those from the lower mantle show elevated R/R_a values up to 40 (Ni et al., 2014; Moore et al., 2017). Helium derived from the Mid-Ocean Ridge Basalt (MORB) displays high isotope ratios with an average (R/R_a) value of about 8. On the other hand, atmospheric He dissolved in the groundwater has an average (R/R_a) value of approximately 1, whereas the crustal-derived He is largely depleted in ^{3}He and therefore has an average value of 0.02 or less (Ballentine et al., 1991).

The relative abundance of some elements such as uranium and thorium in the rock forming minerals determines the extent of He generation from the crustal rocks and

hence controls its average R/R_a values (e.g. Poreda et al. 1986; Darrah et al. 2015; Moore et al. 2017). Pure crustal-derived He commonly shows R/R_a values greater than 0.05 and mixing with mantle-derived He would increase the values up to 0.5 (Ni et al., 2014; Darral e of Mt-Kitty-1 well reve ossibly with atmospheric le depletion relative to ot eflecting the dominant in e (Fig. 20A) coupled wit within the formation wa eham et al., 2018).

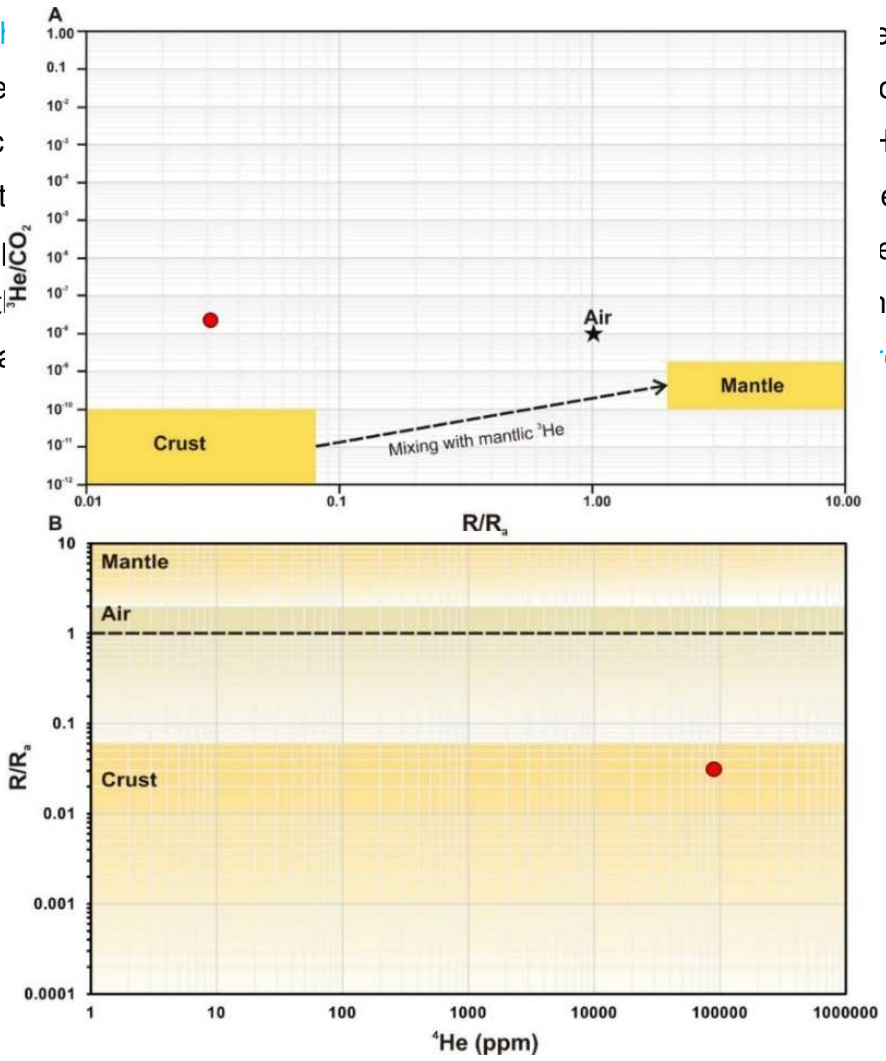

887 **Fig. 20.** (A) Plot of R/Ra ratio versus $^{3}He/CO_2$, (B) ^{4}He versus R/Ra plot illustrating the
888 crustal origin of helium in the studied gases. Data are from McInnes et al. (2017).

889 The log-log plot of R/R_a versus ^{4}He concentration (Fig. 20B) confirms the dominant
890 crustal origin of He in Mt Kitty-1 well. Thus, we hypothesize that He gas accumulation in
891 Mt Kitty-1 well is mostly derived from the sub-salt granitic basement rocks. The spectral
892 gamma ray logs typified that these rocks are rich in uranium and thorium (Fig. 15), thus
893 they are capable of generating helium via radiogenic reactions and radioactive decay
894 these elements. This crustal derivation of He is often coupled with a concomitant
895 generation of H_2 via a radiolytic dissociation of water (e.g. Lin et al., 2005; Warr et al.,
896 2019). Alternatively, H_2 may also be generated by oxidation of iron rich materials but we
897 do not have data on the deepest layer mineralogy to discuss this hypothesis. Another
898 plausible mechanism for H_2 generation is the oxidation of hydrocarbons, however the
899 negative correlation between H_2 and hydrocarbon phases such as CH_4 (R^2= -0.75) as
900 well as the complete absence of H_2 in the above-salt layers of Murphy-1 well may rule
901 out a significant H_2 input via oxidation of HC gases.

902 ### 5.3. Gas accumulation versus gas seepage

903 In the study region, the studied gases are reported from the sub-salt basement and
904 Heavitree Formation. Fractures in the granitic basement present the main gas-bearing
905 zones in Mt Kitty-1 well. Fractures are ubiquitous in the Proterozoic basement rocks
906 paving the base of the Amadeus Basin. The fracture network is commonly controlled by
907 the faults and the high porosities and permeabilities are often associated with the
908 tectonically induced fractures (Heap and Kennedy, 2016). Mt-Kitty-1 well is located in a
909 tectonically-high region due to the tectonic uplift of the faulted basement associated with
910 the fracture patterns and deep-seated faults which are commonly infilled with gases
911 (high resistivity zones) that are sealed beneath the thick Gillen salt layers (Fig. 6).
912 Therefore, gas accumulation in Mt Kitty-1 area are a classical structural trap sealed by
913 the thick salt layers.

914 The porous sandstones of Heavitree Formation present a potential gas pay zone in
915 Magee-1 well. Heavitree Formation has minimal contents of matrix and pore-filling
916 cements and therefore preserves a very good intergranular porosity. The intergranular
917 pores are well-connected and hence display a good effective porosity likely infilled with

gases (Fig. 11). But the Heavitree Formation is very thin in Magee-1 well (< 6 m), and thus hindering any economic accumulation of gases. Moreover, economic gas accumulations should occur in the western and southwestern parts of the basin where the Heavitree Formation is believed to be thicker (Fig. 5B). Additionally, the thickness of the Gillen salt layers also increases westward and southwestward and therefore will provide effective seal for the trapped gasses in the Heavitree pay zone (Fig. 8B).

The above-salt reservoir intervals are scarce and the wireline log results reveal occurrence of thick non-porous and impermeable intervals. However, thin porous and permeable sandstone zones were observed in the Inindia Beds where the effective porosity reaches up to 20%. These zones likely present potential reservoirs for the gaseous hydrocarbons that were generated from the organic-rich zones in Inindia Beds, however its low thickness may hinder any economic gas accumulations in this region.

Gas seepage zones such as SCD are correlated with distribution of the thin salt layers. Observed discrepancies in the seismic reflections (gas chimneys) often coincide with the regions where the thickness of the salt layers is minimal (Fig. 7). Thick accumulation of salt layers commonly provides effective seal for fluids preventing their leakage and hence allows the economic gas accumulation and entrapment in the reservoir rocks (Grunau, 1987; Schlomer and Krooss, 1997). Furthermore, for gases with a relatively small atomic radius such as He and H_2, thick impervious salt layers are essential for to their entrapment in the reservoir. On the other hand, a clear link is observed between the surficial SCD distribution and the subsurface gas chimneys (Fig. 22), and both are correlated with regions where thin layers of Gillen salt exist.

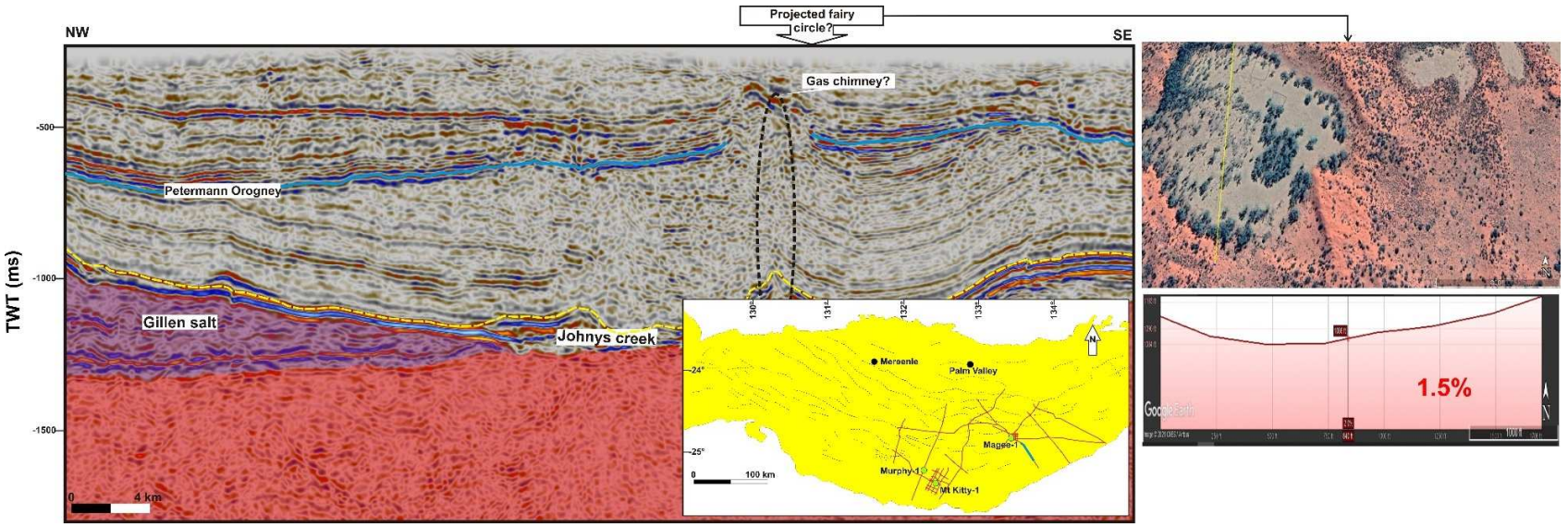

Fig. 21. Interpreted 2D seismic profile illustrating possible occurrence of gas chimneys where the Gillen Salt layers are thinning. The subsurface gas chimneys are well-correlated with SCD typifying continuous gas emanations.

6. Conclusions

- In the Amadeus Basin, hydrocarbon (HC) and non-hydrocarbon gas blend was discovered in some exploratory wells. The gases range from HC-He-rich in Magee-1 to HC-He-H2 blend in Mt Kitty-1 well.
- The HC gases are wet gas with a significant share (> 10%) of C_{2+} components.
- Potential HC-source rock intervals likely occur in the Neoproterozoic Lower Gillen shales, however, the Rock-Eval data revealed a remnant inert carbon with minimal capability to generate HC gases.
- Modeling results shows that wet HC-gases may have been generated from the Lower Gillen shales that had an initial organic carbon of at least 1.3 wt% and entered the gas generation window during Late Devonian at the end of Alice Springs orogeny. The temperatures remain rather low but the 400 years allowed this gas generation.
- He-rich gases display a crustal signature with elevated ^3He contents and R/R_a value of 0.031 typifying their generation via radiolytic decay of the thorium and uranium-rich basement potentially synchronous with H_2 generation from radiolysis. Other source of H_2 by water reduction cannot be precluded.

The Amadeus Basin case study allows to open new horizons since the gas is very likely a classical accumulation, in a structural trap sealed by a salt layer. The reservoir has been charged by these three gases at different rates but probably all over hundreds of millions of years since the He generation is a low process. The presence of this mixture shows that the salt may retain these light gases for millions of years, which opens new exploration perspectives.

Acknowledgment

The authors gratefully acknowledge Emanuelle Frery for the collaboration and the help to collect the Amadeus basin data set. Moreover, some datasets (e.g. 2D seismic) were kindly provided by Geoscience Exploration and Mining Information System (GEMIS) of the Northern Territory, Australia. We thank Dan Levy and Gabriel Pasquet, from E2S UPPA, for many interesting discussions. We appreciate the comments of

Branimir Segvic and another anonymous reviewer that significantly improved the manuscript. This work is a part of Keanu Loiseau master project that has been funded by Engie. A part of the work has also been funded by Campus France in the frame of Make our Planet Great Again “MOPGA” program (project number mopga-pdf-0000000089).

References

Aguilera, R.F., Aguilera, R., 2004. A triple-porosity model for petrophysical analysis of naturally fractured reservoirs”, Petrophysics 45, 157-166.

Allen, A.P., Allen, R.J., 1990. Basin Analysis: Principles and Applications (First ed.). 451 pp. Oxford, Blackwell Scientific Publications.

AMDEL CORE SERVICES, 1993. Petrology and core analysis report of Heavitree sandstone. Prepared for oil Pacific Oil & Gas Ltd., 11 pp, internal report.

Bagas, L., Grey, K., Williams, I.R., 1996. Reappraisal of the Paterson Orogen and Savory Basin, in Geological Survey of Western Australia Annual Review, 55-63.

Ballentine, C. J., O’Nions, R. K., Oxburgh, E. R., Horvath, F., Deak, J., 1991. Rare gas constraints on hydrocarbon accumulation, crustal degassing and groundwater flow in the Pannonian Basin. Earth and Planetary Science Letters 105, 229-246.

Bernard, B., Brooks, J., Sackett, W., 1978. Light hydrocarbons in recent Texas continental shelf and slope sediments. J. Geophys. Res. 83, 4053-4061.

Blamey, N., Brand, U., Parnell, J., Spear, N., Lécuyer, C., Benison, K., Meng, F., Ni, P., 2016. Paradigm shift in determining Neoproterozoic atmospheric oxygen. Geology 44 (8), 651-654.

Blatt, H., Tracy, R. 1996. Petrology: Igneous, Sedimentary, and Metamorphic, Freeman 2nd ed., pp. 518.

Boreham, C., Edwards, D., Poreda, R., Darrah, T., Zhu, R., Grosjean, E., Main, P., Waltenberg, K., Henson, P., 2018. Helium in the Australian liquefied natural gas economy. The APPEA Journal 58, 209-237.

Carr, L.K., Korsch, R.J., Palu, T.J., Reese, B., 2016. Onshore basin inventory: the McArthur, South Nicholson, Georgina, Wiso, Amadeus, Warburton, Cooper and Galilee Basins, central Australia, Geoscience Australia Record 2016/04.

Charlou, J.L., Donval, J.P., Fouquet, Y., Jean-Baptiste, P., Holm, N., 2002. Geochemistry of high H2 and CH4 vent fluids issuing from ultramafic rocks at the Rainbow hydrothermal field (36◦14\ N, MAR). Chem. Geol. 191, 345-359.

Combaudon, V., I Moretti, B. Kleine, A Stefánsson. 2022. Natural hydrogen emissions in Iceland and comparison with the Mid-Atlantic Ridge. Int. J. Hydrog. Energy 47, 10217-10227.

Coveney, R., Goebel, E., Zeller, E., Dreschhoff, G.A.M., Angino, E.E., 1987. Serpentinization and origin of hydrogen gas in Kansas. AAPG Bull. 71, 39-48.

Darrah, T. H., Jackson, R. B., Vengosh, A., Warner, N. R., Whyte, C. J., Walsh, T. B., Kondash, A. J., Poreda, R. J., 2015. The evolution of Devonian hydrocarbon gases in shallow aquifers of the northern Appalachian Basin: insights from integrating noble gas and hydrocarbon geochemistry. Geochimica et Cosmochimica Acta 170, 321-355.

Edgoose, C.J., 2013. Amadeus Basin, In Ahmad, M., Munson, T.J. (Eds.), Geology and mineral resources of the Northern Territory, Northern Territory Geological Survey, Special Publication 5, 23-70.

Espitalié, J., Deroo, G., Marquis, F., 1986. Rock–Eval pyrolysis and its applications. Part III. Revue de l'Institut Franc¸ais du Pe´trole 41, 73-89.

Etiope, G., 2017. Abiotic methane in continental serpentinization sites: an overview. Proc. Earth Planet. Sci. 17, 9-12.

Frery, E., Langhi, L., Maison, M., Moretti, I., 2021. Natural hydrogen seeps identified in the North Perth Basin, Western Australia. Int. J. Hydrog. Energy 46, 31158-31173.

Geotech, 1992. Source rock chracterization study Magee-1. Prepared for oil Pacific Oil & Gas Ltd., 11 pp, internal report.

Geymond, U., Ramanaidou, E., Lévy, D., Ouaya, A., Moretti, I., 2022. Can weathering of Banded Iron Formations generate natural hydrogen? Evidences from Australia, Brazil and South Africa. Minerals, 12, 163. https://doi.org/10.3390/xxxxx

Gielen, D., Boshell, F., Saygin, D., Bazilian, M., Wagner, N., Gorini, R., 2019. The role of renewable energy in the global energy transformation. Ener. Strat. Rev. 24, 38-50.

Grunau, H.R., 1987. A worldwide look at the caprock problem. J. Petrol. Geol. 10, 245-266.

Haines, P.W., Allen, H-J. A., 2019. Hydrocarbon and helium prospectivity of the Amadeus and Murraba basins in Western Australia, in Keep, M., Moss, S.J. (Eds.), The Sedimentary Basins of Western Australia V: Proceedings of the Petroleum Exploration Society of Australia Symposium, Perth, WA, 2019, 17 pp.

Haines, P.W., Wingate, M.T.D., Kirkland, C.L., Allen, H.J., 2015, Detrital zircon geochronology of upper Ediacaran to lower Cambrian deposits (Supersequence 4), western Amadeus Basin: Testing revised stratigraphic correlations, Geological Survey of Western Australia Record 2015/8.

1048 Heap, M., Kennedy, B., 2016. Exploring the scale-dependent permeability of fractured andesite.
1049 Ear. Plan. Sci. Lett. 447, 139-150.
1050 Herron, D.A., 2011. First Steps in Seismic Interpretation. Society of Exploration Geophysicists.
1051 Hissey, E., Clifford, J., Debacker, T., 2016, Exploring the sub-salt play in the frontier Amadeus
1052 Basin –insights from regional 2D seismic and potential field data, in 25th International
1053 Geophysical Conference and Exhibition, Adelaide, South Australia, Australian Society of
1054 Exploration Geophysicists, Extended Abstracts, 111-118.
1055 Holloway, J., O'Day, P., 2000. Production of CO2 and H2 by diking-eruptive events at Mid-
1056 Ocean Ridges: Implications for abiotic organic synthesis and global geochemical cycling.
1057 Int. Geol. Rev. 42, 673-683.
1058 Hunt, J.M., 1996. Petroleum Geochemistry and Geology, second ed. W.H. Freeman and
1059 Company, New York, p. 743.
1060 Jackson, K.S., McKirdy, D.M., Deckelman, J.A., 1984. Hydrocarbon generation in the Amadeus
1061 Basin, central Australia. The APEA Journal 24(1), 42-65.
1062 Johns, D. R., Menpes, S. A.,Walshe, P., Bache, F., 2017. Exploration of a sub-salt play in the
1063 southernAmadeus Basin, CentralAustralia – searching for big gas in Proterozoic
1064 reservoirs. Proceedings of the 2017 South East Asia Petroleum Exploration Society
1065 (SEAPEX) Conference, 2017, Abstract: http://archives.datapages.com/data/southeast-
1066 asia-petroleumexploration-society/data/028/028001/3a_seapex0280003a.htm. Available
1067 at https://centralpetroleum.com.au/wp-content/uploads/2016/10/ Santos-Seapex-
1068 Presentation-AMADEUS-Johns-et-al-2017.pdf.
1069 Klein F, Tarnas J, Bach W. Abiotic sources of molecular hydrogen on earth. Elements
1070 2020;16:19e24. https://doi.org/ 10.2138/gselements.16.1.19.
1071 Larin, N., Zgonnik, V., Rodina, S., Deville, E., Prinzhofer, A., Larin, V.N., 2015. Natural
1072 molecular hydrogen seepage associated with surficial, rounded depressions on the
1073 European craton in Russia. Nat. Resour. Res. 24(3), 369-383.
1074 Leila, M., Levy, D., Battani, A., Piccardi, L., Segvic, B., Badurina, L., Pasquet, G., Combaudon,
1075 V., Moretti, I., 2021. Origin of continuous hydrogen flux in gas manifestations at the
1076 Larderello geothermal field, Central Italy. Chem. Geol. 585, 120564.
1077 Leila, M., Moscariello, A., 2017. Organic geochemistry of oil and natural gas in the West Dikirnis
1078 and El-Tamad fields onshore Nile Delta, Egypt: Interpretation of potential source rocks.
1079 J. Petrol. Geol., 40, 37-58.

Lin, L., Slater, G.F., Lollar, B.S., Lacrampe-Couloume, G., Onstott, T.C., 2005. The yield and isotopic composition of radiolytic H2, a potential energy source for the deep subsurface biosphere. Geochim. Cosmochim. Acta 69 (4), 893-903.

Lopatin, N. V., 1971. Temperature and geologic time as factors in coalification (in Russian). Akademiya Nauk SSSR Izvestiya, Seriya Geol. 3, 95-106.

Marshall, T.R., 2003. Petroleum systems and source rocks in the Amadeus Basin, Northern Territory, In Cowie, M., (Ed.), Queensland 2003 exploration and development. Petroleum Exploration Society of Australia (Qld/NT) 2003 Symposium, 37-42.

Marshall, T.R., 2004, A review of source rocks in the Amadeus Basin. Northern Territory Geological Survey, Record 2004-008.

Marshall, T.R., Dyson, I.A., Liu, K., 2007, Petroleum systems in the Amadeus Basin, central Australia: Were they all oil prone?, In Munson, T.J., Ambrose, G.J. (Eds.), Central Australian Basins Symposium, Northern Territory Geological Survey Special Publication 2, 136-146.

McCollom, T.M., Bach, W., 2009. Thermodynamic constraints on hydrogen generation during serpentinization of ultramafic rocks. Geochim. Cosmochim. Acta 73, 856-875.

McInnes, B., Darrah, T., Hilton, R., Boreham, C., Edwards, D., Gusterhuber, J., 2017. Investigations into the highest reported He concentration in a natural gas sample: Mt Kitty, Amadeus Basin, Northern Territory. In: Abstract at Goldschmidt 2017 Conference, Paris, France, August 13-18, 2017. https://goldschmidt.info/2017/abstracts/abstractView?id=2017003781.

Moore, M. T., Vinson, D. S., Whyte, C. J., Eymold, W. K., Walsh, T. B., Darrah, T. H., 2017. Differentiating between biogenic and thermogenic sources of natural gas in coalbed methane reservoirs from the Illinois Basin using noble gas and hydrocarbon geochemistry. In Lawson, M., Formolo, M., J.M. Eiler, J.M., (Eds.), From Source to Seep: Geochemical Applications in Hydrocarbon Systems. Geological Society, London, Special Publications, 468.

Moretti, I., Brouilly, E., Loiseau, K., Prinzhofer, A., Deville, E., 2021b. Hydrogen emanations in intracratonic areas: New guide lines for early exploration basin screening. Geosci., 11 (3), 145.

Moretti, I., Prinzhofer, A., Francolin, J., Pacheco, C., Rosanne, M., Rupin, F., Mertens, J., 2021a. Long-term monitoring of natural hydrogen superficial emissions in a brazilian cratonic environment. Sporadic large pulses versus daily periodic emissions. Int. J. Hydrog. Energy 46, 3615-3628.

Ni, Y., Dai, J., Tao, S., Wu, X., Liao, F., Wu, W., Zhang, D., 2014. Helium signatures of gases from the Sichuan Basin, China. Org. Geochem. 74, 33-43.

Orlando, A., Maria Conte, A., Borrini, D., Perinelli, C., 2010. Exprimental investigation of CO2-rich fluids production in a geothermal area: the Mt Amiata (Tuscany, Italy) case study. Chem. Geol. 274, 177-186.

Pepper, S.A., Corvi, J.P., 1995. Simple kinetic models of petroleum formation. Part I: oil and gas generation from kerogen. Mar. Petrol. Geol. 12, 291-319.

Peters, K.E., Cassa, M.R., 1994. Applied source rock geochemistry. In Magoon, L.B., and Dow, W.G. (Eds.), The petroleum system from source to trap (93-117), AAPG, Tulsa, Oklahoma.

Peters, E.K., Walters, C.C., Moldowan, M.J., 2005. The Biomarker guide 2nd Edition. Volume I: Biomarkers and Isotopes in the Environment and Human History). 471 pp. Cambridge, Cambridge University Press.

Peters, K.E., 1986. Guidelines for evaluating petroleum source rock using programmed pyrolysis. AAPG Bull. 70, 318-329.

Powell, C., Preiss,W.V., Gatehouse, C.G., Krapez, B., LI., Z.X., 1994, South Australian record of a Rodinian epicontinental basin and its mid-Neoproterozoic breakup (~700 Ma) to form the Palaeo-Pacific Ocean, Tectonophysics 237, 113–140. https://doi. org/10.1016/0040-1951(94)90250-X.

Poreda, R. J., Jenden, P. D., Kalpan, I. R., Craig, H., 1986. Mantle helium in Sacramento Basin natural gas wells. Geochimica et Cosmochimica Acta 50, 2847-2853.

Prinzhofer, A., Moretti, I., Françolin, J., Pacheco, C., D'Agostino, A., Werly, J., Rupin, F., 2019. Natural hydrogen continuous emission from sedimentary basins: the example of a Brazilian H2-emitting structure. Int. J. Hydrog. Energy 44, 5676-5685.

Prinzhofer, A., Tahara Cissé, C.S., Diallo, A.B., 2018. Discovery of a large accumulation of natural hydrogen in Bourakebougou (Mali). Int. J. Hydrog. Energy 43, 19315-19326.

Qin, S., Zhang, Y., Zhao, C., Zheng Zhou, Z., 2018. Geochemical evidence for in situ accumulation of tight gas in the Xujiahe Formation coal measures in the central Sichuan Basin, China. Int. J. Coal Geol. 196, 173-184.

Qin, S., Chunhu, H., Benjian, Z., Yu, Y., Miao, Y., 2019. Relationships of the iC4/nC4 and iC5/nC5 ratios with maturity of coal-derived gases of Triassic Xujiahe Formation in central Sichuan Basin, SW China. Petrol. Expl. Develop. 46(3), 496-503.

1146 Radwan, A., Nabawy, B., Shihata, M., Leila, M., 2022. Seismic interpretation, reservoir
1147 characterization, gas origin and entrapment of the Miocene-Pliocene Mangaa C
1148 sandstone, Karewa Gas Field, North Taranaki Basin, New Zealand
1149 Schlomer, S., Krooss, B., 1997. Experimental characterization of the hydrocarbon sealing
1150 efficiency of cap rocks. Mar. Petrol. Geol. 14, 565-580.
1151 Schoell, M., 1983. Genetic characterization of natural gases. AAPG Bull. 67 (12), 2225-2238.
1152 Scrimgeour, I.R., 2019, Overview of mineral and petroleum exploration and production in 2018,
1153 Annual Geoscience Exploration Seminar Proceedings, Northern Territory Geological
1154 Survey, 1-14.
1155 Sherwood Lollar, B., Onstott, T.C., Lacrampe-Couloume, G., Ballentine, C.J., 2014. The
1156 contribution of the Precambrian continental lithosphere to global H2 production. Nature
1157 516, 379-382.
1158 Skirrow, R. G., Huston, D. L., Mernagh, T. P., Thorne, J. P., Dulfer, H., Senior, A. B., 2013.
1159 Critical commodities for a high-tech world: Australia's potential to supply global demand.
1160 Geoscience Australia, Canberra. Available at https://ecat.ga.gov.au/geonetwork/srv/eng/
1161 search#!dfdb8e16-3c25-0990-e044-00144fdd4fa6.
1162 Stack, S., Rabone, H., 2018. Cobar Management Pty Ltd: the CSA mine annual environmental
1163 management report. AEMR 2017. http://www.csamine.com.au/u
1164 ploads/51687/ufiles/CSA-AEMR_2017_-_Final_opt.pdf.
1165 Stefánsson, A., Arnórsson, S., 2002. Gas pressures and redox reactions in geothermal fluids in
1166 Iceland. Chem. Geol. 190, 251-271.
1167 Summons, R.E., Powell, T.G., 1991. Petroleum source rocks of the Amadeus Basin. Bureau of
1168 Mineral Resources, Australia, Bull. 236, 511-523.
1169 Sweeney, J.J., Burnham, K.A., 1990. Evaluation of a simple model of vitrinite reflectance based
1170 on chemical kinetics. AAPG Bull. 74(10), 1559-1570.
1171 Tao, S., Zou, C., Mi, J., Gao, X., Yang, C., Zhang, X., Fan, J., 2014. Geochemical comparison
1172 between gas in fluid inclusions and gas produced from the Upper Triassic Xujiahe
1173 Formation, Sichuan Basin, and SW China. Org. Geochem. 74, 59-65.
1174 Taran, Y.A., Varley, N.R., Inguaggiato, S., Cienfuegos, E., 2010. Geochemistry of H2- and CH4-
1175 enriched hydrothermal fluids of Socorro Island, Revillagigedo Archipelago, Mexico.
1176 Evidence for serpentinization and abiogenic methane. Geofluids 10, 542-555.
1177 Tissot, B., Welte, D., 1984. Petroleum Formation and Occurrence. Springer-Verlag, New York,
1178 p. 699.

Truche, L., McCollom, T., Martinez, I., 2020. Hydrogen and Abiotic Hydrocarbons: Molecules that Change the World. Elements 16 (1), 13-18.

Ungerer, P., 1990. State of the art research in kinetic modeling of oil formaion and expulsion. Org. Geochem., 16(1-3), 1-25.

Vacquand, C., Deville, E., Beaumont, V., Guyot, F., Sissmann, O., Pillot, D., Arcilla, C., Prinzhofer, A., 2018. Reduced gas seepages in ophiolitic complexes: evidences for multiple origins of the H2-CH4-N2 gas mixtures. Geochim. Cosmochim. Acta 223, 437-461.

Waltenberg, K., 2015, Helium as a critical commodity: opportunities in the Northern Territory, Annual Geoscience Exploration Seminar Proceedings, Northern Territory Geological Survey Record 2015-002, p. 92.

Walter, M.R., Veevers, J.J., Calver, C.R., Grey,K., 1995, Neoproterozoic stratigraphy of the Centralian Superbasin, Australia, Precambrian Research 73, 173-195. https://doi.org/10.1016/0301-9268(94)00077-5.

Wang, P., Shen, Z.,He, C., 2017. The geochemical characteristics of butane and its application. Natural Gas Geoscience 28(4), 529-538.

Waples, D., 1980. Time and temperature in petroleum generation and application of Lopatin's technique to petroleum exploration. AAPG Bull. 64, 916-926.

Watson, M. N., Boreham, C. J., Tingate, P. R., 2004. Carbon dioxide and carbonate cements in the Otway Basin: implications for geological storage of carbon dioxide. The APPEA Journal 44(1), 703-720.

Warr, O., Giunta, T., Ballentine, C., Sherwood, B., 2019. Mechanisms and rates of 4He, 40Ar, and H2 production and accumulation in fracture fluids in Precambrian Shield environments. Chem. Geol. 530, 119322. https://doi.org/10.1016/j.

Wells, A.T., Forman, D.J., Ranford, L.C., Cook, P.J., 1970, Geology of the Amadeus Basin, central Australia. Bureau of Mineral Resources, Geology and Geophysics, Bull. 100, pp. 282.

Whiticar, M., 1999. Carbon and hydrogen isotope systematics of bacterial formation and oxidation of methane. Chem. Geol. 161, 291-314.

Wood, D., 2018. Thermal maturity and burial history modelling of shale is enhanced by use of Arrhenius time-temperature index and memetic optimizer. Petroleum 4, 25-42.

Woolnough, W.G., 1934. Natural gas in Australia and New Guinea. AAPG bull., 18, 226-242.

1211 Wygrala, B.P., 1989. Integrated study of an oil field in the southern Po basin, northern Italy.
1212 Unpublished Dissertation thesis, Berichte Kernforschungsanlage Jülich, University of
1213 Köln, Köln. 217 pp.
1214 Young, I.F., Ambrose, G.J., 2007, Petroleum geology of the southeastern Amadeus Basin: The
1215 search for sub-salt hydrocarbons, In MUNSON, T.J., AMBROSE, G.J. (Eds.,), Central
1216 Australian Basins Symposium, Northern Territory Geological Survey Special Publication
1217 2, 183-204.
1218 Zgonnik, V., 2020. The occurrence and geoscience of natural hydrogen: a comprehensive
1219 review. Earth Sci. Rev. 203, 103140.
1220 Zgonnik, V., Beaumont, V., Deville, E., Larin, N., Pillot, D., Farrell, K.M., 2015. Evidence for
1221 natural molecular hydrogen seepage associated with Carolina bays (surficial, ovoid
1222 depressions on the Atlantic Coastal Plain, Province of the USA). JPiE and Science P,
1223 2(1), 31.

Table 1. Total organic carbon (TOC) and Rock-Eval pyrolysis results for the analyzed shale samples retrieved from the studied wells in Amadeus Basin.

Well name	Formation	Depth (m)	TOC (wt%)	PC (wt%)	S1 mg/g	S_2 mg/g	S_3 mg/g	T_{max} (C°)	HI	OI	PI	GP
Magee-1	U. Gillen	1927	0.52	0.07	0.35	0.47	0.47	393	90	903	0.43	0.82
Magee-1	U. Gillen	2217	0.49	0.28	2.65	0.78	0.60	350	159	122	0.77	3.43
Magee-1	L. Gillen	2323	0.79	0.05	0.18	0.45	0.27	442	57	34	0.29	0.63
Magee-1	L. Gillen	2326	0.81	0.05	0.20	0.41	0.27	445	51	33	0.33	0.61
Magee-1	L. Gillen	2329	0.53	0.03	0.10	0.28	0.24	444	53	45	0.26	0.38
Magee-1	L. Gillen	2332	0.63	0.03	0.09	0.33	0.24	441	52	38	0.21	0.42
Magee-1	L. Gillen	2335	0.49	0.02	0.06	0.21	0.20	442	43	41	0.22	0.27
Magee-1	L. Gillen	2338	0.60	0.04	0.11	0.36	0.21	442	60	35	0.23	0.47
Magee-1	L. Gillen	2341	0.50	0.03	0.09	0.31	0.15	444	62	30	0.23	0.40
Magee-1	L. Gillen	2344	0.45	0.02	0.05	0.14	0.18	393	31	40	0.26	0.19
Murphy-1	Inindia Beds	1005	2.29	0.05	0.13	0.49	0.04	433	21	2	0.21	0.62
Murphy-1	Inindia Beds	1056	3.19	0.06	0.16	0.53	0.06	435	17	2	0.23	0.69

TOC = total organic carbon. S_1 = volatile hydrocarbon content (mg HC/g rock); S_2 = remaining hydrocarbon generative potential (mg HC/g rock); S_3 = carbon dioxide yield (mg CO_2/g rock); T_{max} = temperature at maximum of S2 peak; HI = hydrogen index (S_2 × 100/TOC) (mg HC/g TOC); OI = oxygen index (S_3 × 100/TOC) (mg CO_2/g TOC); PI = production index (S_1/ (S_1 + S_2)); GP = Generation potential (S_1 + S_2) (mg/g).

Table 2. Composition of the analyzed gas blend collected from the studied wells in Amadeus Basin. isotope gas analyses are reported from McInnes et al. (2017).

Well name	Depth (m)	N_2	Ar	He	H_2	CO_2	C_1	C_2	C_{2+}	IC_4/ nC_4	IC_5/ nC_5	DC	R/R_a	CO_2/ ^3He	^{84}Kr/ ^{36}Ar	^{132}Xe/ ^{84}Kr
Magee-1	2349	43.61	0.46	6.20	0.03	0.82	39.26	6.10	3.52	0.63	1.11	0.80	-	-	-	-
Mt Kitty-1	2144	79.62	-	4.23	5.05	0.33	7.29	2.10	2.85	0.41	8.00	0.71	-	-	-	-
Mt Kitty-1	2156	61.04	0.57	8.96	11.4	0.09	13.14	3.53	1.24	0.36	6.50	0.73	0.031*	4.46 x 10^{7}*	0.0062*	0.142*
Mt Kitty-1	2253	99.67	-	0.0	0.0	0.08	0.04	0.02	0.01	0	0	-				
Murphy-1	1647	-	-	-	-	-	1.18	0.01	0.31	0	0	0.79				
Murphy-1	1650	-	-	-	-	-	32.69	2.87	3.90	1.08	0.96	0.83				
Murphy-1	1653	-	-	-	-	-	72.61	3.21	0.99	1.10	0.25	0.94				
Murphy-1	1656	-	-	-	-	-	27.81	3.14	3.61	1.30	0.82	0.81				
Murphy-1	1764	-	-	-	-	-	1.48	0.08	0.16	0	0	0.90				

*Dc is the dryness Coefficient ($C_1/\Sigma C_1$-C_3); * Noble gas data is from (McInnes et al., 2017).*